https://doi.org/10.5194/egusphere-2026-3865
Preprint. Discussion started: 7 August 2026

Investigating ice microphysical processes in the dendritic growth zone by combining Monte-Carlo Lagrangian particle modelling with multi-frequency polarimetric radar observations

Leonie von Terzi[1], Axel Seifert[2], Christoph Siewert[2], Fabian Jakub[2], and Stefan Kneifel[1]
[1]Ludwig-Maximilians University Munich
[2]Deutscher Wetterdienst
Correspondence: Leonie von Terzi (L.Terzi@lmu.de)

Abstract.
The dendritic growth zone (DGZ) is associated with distinct polarimetric and multi-frequency radar signatures, yet governing microphysical processes remain uncertain. We analyse DGZ observations showing a concurrent increase in dual-wavelength ratio (DWR), enhanced specific differential phase shift (KDP) and the maximum of the spectrally resolved ZDR ($sZDR_{max}$), a pronounced reduction in mean Doppler velocity (MDV), and the occurrence of a secondary Doppler spectral mode near $-15\,^{\circ}$C.

To investigate the governing processes, radar observations are combined with the Lagrangian particle-based Monte Carlo model McSnow, which includes an updated ice habit scheme and a new fragmentation parametrization. Forward radar simulations use a discrete dipole approximation scattering database.

The simulations show that enhanced $sZDR_{max}$ requires local formation of dendritic or plate-like crystals near $-15\,^{\circ}$C; sedimentation of pre-existing particles alone cannot reproduce the signal. The KDP enhancement is only reproduced when secondary ice production via collisional fragmentation is included, which also strengthens aggregation-related signatures. The reduction in mean Doppler velocity is explained by a habit change and aggregation of sedimenting columnar ice particles. Together, these signatures provide the most diagnostic constraints on DGZ microphysical processes identified so far.

This study demonstrates that multi-frequency polarimetric radar observations combined with Monte Carlo Lagrangian particle simulations can disentangle competing microphysical processes in the DGZ. The results identify collisional fragmentation as a key unifying mechanism, with the DGZ radar fingerprint emerging from the interplay of depositional growth, aggregation, and secondary ice production.

1 Introduction

Ice-phase processes in clouds play a central role in the formation of precipitation, with more than 70% of global precipitation generated through the ice phase (Heymsfield et al., 2020; Field and Heymsfield, 2015; Mülmenstädt et al., 2015). Among the temperature regimes relevant for ice growth, the dendritic growth zone (DGZ), located between -20 and $-10\,^{\circ}$C, is of particular importance because several key microphysical processes reach peak efficiency in this temperature range.

https://doi.org/10.5194/egusphere-2026-3865
Preprint. Discussion started: 7 August 2026

The microphysical importance of the DGZ arises from a combination of thermodynamic and habit-dependent growth effects. Near $-12\,^{\circ}\mathrm{C}$, the difference between saturation vapour pressure over water and ice reaches a maximum, favouring rapid depositional growth via the Wegener–Bergeron–Findeisen process (Korolev, 2007). In addition, ice crystals preferentially grow into plate-like and dendritic habits in this temperature range, leading to a pronounced maximum in depositional growth rates around $-15\,^{\circ}\mathrm{C}$ (Takahashi, 2014). The resulting fragile, branched structures enhance susceptibility to breakup, making the DGZ a potential hotspot for secondary ice production (SIP) (Takahashi et al., 1995; Phillips et al., 2018; Grzegorczyk et al., 2023; Gautam et al., 2024). SIP and particularly collisional ice fragmentation have received increasing attention as a possible explanation for the frequently observed discrepancy between ice-nucleating particle concentrations and ice particle number concentrations in clouds (Kanji et al., 2017; Georgakaki et al., 2022).

Rapidly growing ice particles in the DGZ are also known to form aggregates very efficiently. The branched geometry of dendritic crystals increases inter-particle stickiness, promoting the formation of large aggregates (Connolly et al., 2012; Lamb and Verlinde, 2011). The coexistence of rapid depositional growth, secondary ice formation, and aggregation makes the DGZ a region where several interacting processes act simultaneously, complicating both observational interpretation and model representation.

Radar observations provide an integrated view of these interacting processes. Typical radar features observed by ground-based cloud radars in the DGZ are shown exemplarily in Figure 1. The profiles represent statistics of several ice and mixed-phase clouds similar to what was presented in von Terzi et al. (2022) and described in more detail in Section 2.1. The statistics are conditioned on periods exhibiting pronounced polarimetric signals within the DGZ, defined here by a maximum W-band KDP exceeding $(1^{\circ}\mathrm{km}^{-1})$. Consequently, the profiles shown in Figure 1 are not intended to represent average DGZ conditions. Instead, they highlight situations characterized by particularly strong polarimetric signatures, thereby sharpening the characteristic DGZ radar fingerprint and facilitating a clearer interpretation of the otherwise complex set of radar observables. Such high-KDP periods account for approximately one quarter of the available observations in our dataset, indicating that the conditions discussed here are common, although not ubiquitous. For the statistics, only profiles which are continuous in the DGZ are considered.

A common feature of DGZ observations is a continuous increase in radar reflectivity toward warmer temperatures, reflecting the combined effects of depositional growth and aggregation (Schrom and Kumjian, 2016; Zawadzki, 2013). This particle growth is often more clearly captured by the dual-wavelength ratio (DWR), which typically exhibits a pronounced increase within the DGZ and is generally interpreted as evidence for rapid particle growth and enhanced aggregation efficiency (Dias Neto et al., 2019; Matrosov, 1992; Kneifel et al., 2015). The strongest DWR increases are frequently observed near temperatures favourable for dendritic crystal growth, where the branching structure of dendrites promotes efficient particle sticking and aggregate formation (Connolly et al., 2012; Lamb and Verlinde, 2011).

Another recurring feature is a reduction in mean Doppler velocity (MDV) within the DGZ. Although fall velocities generally increase as particles grow while descending through a cloud, numerous studies have reported a localized slowdown coincident with enhanced dendritic growth (e.g. von Terzi et al., 2022; Schrom and Kumjian, 2016; Schrom et al., 2015; Zawadzki, 2013). Similar signatures have also been identified in spectrally resolved observations, where the slowdown tends to be most pro-

https://doi.org/10.5194/egusphere-2026-3865
Preprint. Discussion started: 7 August 2026

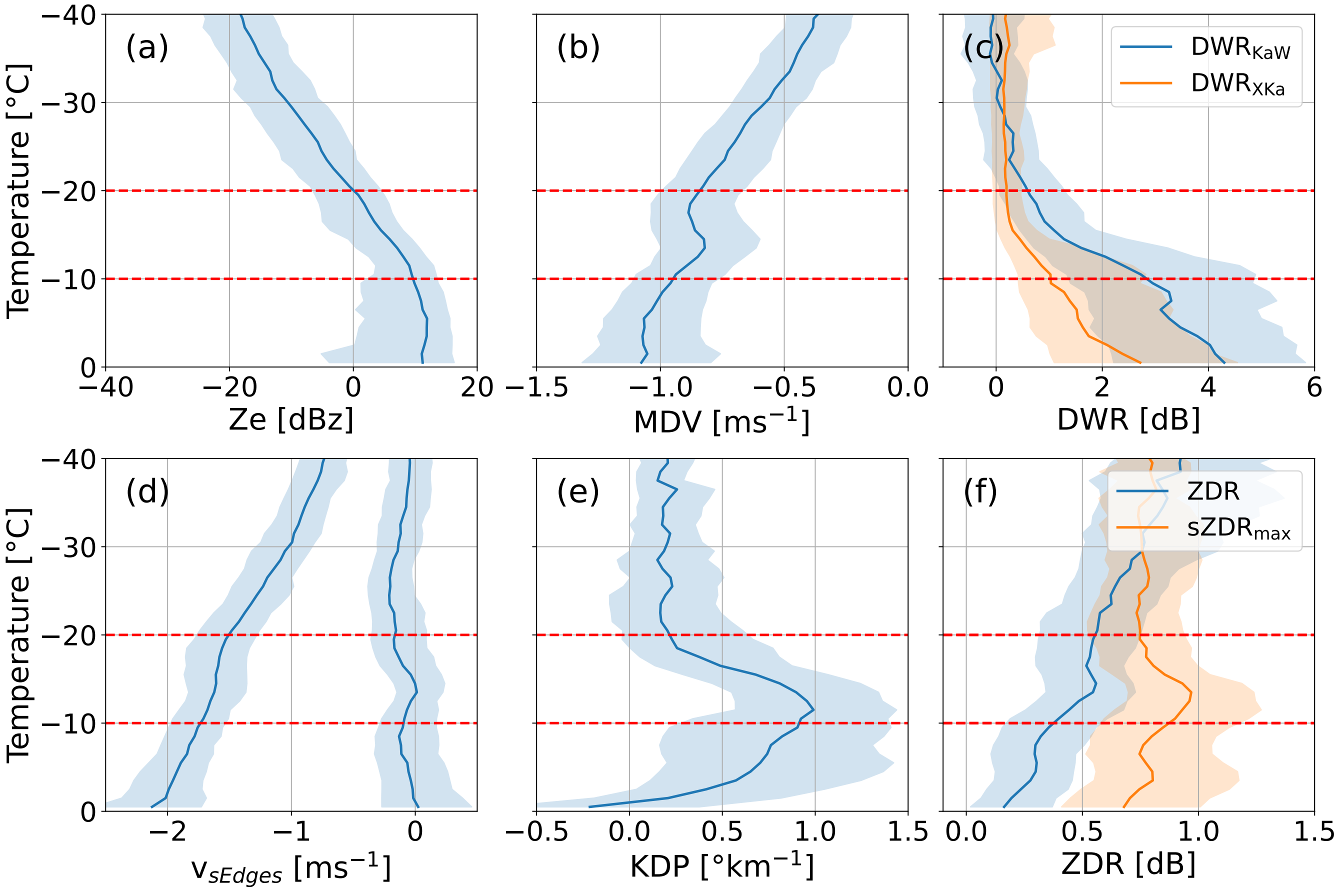

Figure 1. Median (solid line), 25$^{\mathrm{th}}$, 75$^{\mathrm{th}}$ percentiles (shaded area around median) of all continuous profiles of the Tripex-pol and Tripex-pol-scan campaign where the maximum of KDP exceeds 1°km^{-1} within the DGZ. The DGZ is indicated by the red dashed lines. Shown are Ze at Ka-Band (a), MDV at Ka-Band (b) $\mathrm{DWR_{KaW}}$ and $\mathrm{DWR_{XKa}}$ (c), slow and fast edges of the Doppler spectrum at Ka-Band (defined as the velocity 3dBz above the noise level) (d), KDP at W-band and 30° elevation (e), as well as ZDR and $\mathrm{sZDR_{max}}$ (defined as the maximum ZDR per height in the spectrally resolved ZDR) at W-Band and 30° elevation (f).

https://doi.org/10.5194/egusphere-2026-3865
Preprint. Discussion started: 7 August 2026

nounced among slowly falling particles. These observations have been interpreted as evidence for either dynamical influences (Zawadzki, 2013), such as localized updrafts, or the emergence of a secondary population of slowly falling ice particles (Oue et al., 2018; Moisseev et al., 2015; Shupe and Intrieri, 2004; Zawadzki et al., 2001; Field, 2000).

Polarimetric radar variables provide additional information on particle shape and orientation. Enhanced differential reflectivity (ZDR) near dendritic growth temperatures is commonly associated with populations of horizontally oriented, high-aspect-ratio ice crystals (e.g. Kumjian, 2013; Griffin et al., 2018; Schrom and Kumjian, 2016; Schrom et al., 2015; Thompson et al., 2014; Bechini et al., 2013; Andrić et al., 2013). As aggregation becomes increasingly important at warmer temperatures, bulk ZDR generally decreases as larger and more isotropic aggregates begin to dominate the radar signal (Kumjian, 2013). Spectrally resolved polarimetric observations have further shown that elevated ZDR values can persist within specific fall-velocity ranges even when the bulk signal is dominated by aggregates, suggesting the continued presence of pristine or weakly aggregated dendritic crystals alongside larger particles (von Terzi et al., 2022; Kötsche et al., 2025).

Similarly, enhanced KDP has frequently been observed within the DGZ and is generally interpreted as evidence for elevated concentrations of small, non-spherical ice particles (Bringi and Chandrasekar, 2001; Kumjian, 2013). Studies reporting strong KDP signatures often also report enhanced DWR, reduced MDV, and elevated spectral polarimetric signatures, indicating that these variables form a coherent set of observational features associated with dendritic growth (e.g. von Terzi et al., 2022; Oue et al., 2018). Together, these recurring signatures constitute a characteristic DGZ radar fingerprint that has been documented across a wide range of cloud regimes and observational campaigns.

Despite the consistency of these observational fingerprints, their physical interpretation remains uncertain. Several mechanisms have been proposed to explain the coexistence of enhanced KDP, elevated DWR, reduced MDV, and distinct Doppler spectral signatures, including localized updrafts associated with enhanced ice nucleation (Zawadzki, 2013), secondary ice production near $-15°$C (e.g. Kennedy and Rutledge, 2011; von Terzi et al., 2022), and sedimentation of small particles into the DGZ which grow via deposition in the favourable environment at $-15°$C (e.g. Moisseev et al., 2015). Because multiple processes may produce similar radar signatures (e.g. Dunnavan et al., 2022), observations alone are often insufficient to distinguish between competing explanations.

In this study, we investigate these scenarios using a process-resolving modelling framework. A new ice-fragmentation parametrization has been implemented within the Lagrangian Monte-Carlo particle microphysical model McSnow (Brdar and Seifert, 2018), enabling explicit representation of collisional breakup in the DGZ. Lagrangian particle-based models are particularly well suited for this problem because they explicitly track the evolution of individual ice particles and aggregates through a multidimensional microphysical phase space. In contrast to traditional bulk or bin schemes, particle properties such as mass, density, habit, aggregate structure, and fall velocity evolve continuously and remain directly linked to the underlying growth, aggregation, fragmentation, and sedimentation processes (Brdar and Seifert, 2018; Morrison et al., 2020). This makes them especially suitable for studies in which multiple radar observables are used simultaneously, as these observables are jointly sensitive to different moments of the particle size, shape, and velocity distributions rather than bulk quantities alone. Combined with the habit prediction scheme of Welss et al. (2023) and radar forward simulations based on a large discrete-dipole approximation (DDA, (Draine and Flatau, 1994)) scattering database (von Terzi et al., 2026), McSnow provides a physically consistent

https://doi.org/10.5194/egusphere-2026-3865
Preprint. Discussion started: 7 August 2026

framework for connecting microphysical process hypotheses directly to observed polarimetric, spectral, and multi-frequency radar signatures. By simulating an intensely observed DGZ case and systematically evaluating the proposed mechanisms, we assess which processes can reproduce the observed combination of KDP, ZDR, DWR, MDV, and Doppler spectral characteristics, thereby improving the physical interpretation of radar observations in the dendritic growth zone.

2 Methods

2.1 Observations

The observations used in this study were collected during the TRIPEx-pol-scan campaign, which followed the earlier TRIPEx (Dias Neto et al., 2019) and TRIPEx-pol (von Terzi et al., 2022) campaigns. As in TRIPEx-pol, the Joyrad-10 (X-band), Joyrad-35 (Ka-band), and the polarimetric W-band radar were co-located on the rooftop platform of JOYCE-CF (Löhnert et al., 2015). A detailed description of these radar systems is provided in von Terzi et al. (2022).

Unlike in TRIPEx-pol, where the Ka-band radar continuously pointed vertically (zenith), the TRIPEx-scan campaign involved coordinated scanning by both the Ka-band and polarimetric W-band radars. This setup enabled the collection of dual-frequency data during synchronized scans. Moreover, TRIPEx-scan placed greater emphasis on slanted observations, which extended the periods of polarimetric radar measurements.

For this study, the relevant data include zenith observations and slant observations conducted at a fixed 30° elevation angle and 315° azimuth angle (hereafter denoted as constant elevation CEL). Both the Ka- and W-band radars were at constant elevation four times per hour. The W-band radar scanned for 6 minutes and the Ka-band for 5 minutes during each interval, beginning at 5, 21, 35, and 50 minutes past the hour. These scans were typically followed by zenith observations.

The Ka-band radar conducted zenith measurements four times per hour, each lasting 4 to 5 minutes (at 10, 26, 40, and 56 minutes past the hour). The W-band radar performed three zenith scans per hour, each lasting 5 minutes (at 10, 40, and 55 minutes past the hour). Following the zenith scans, both radars executed Range Height Indicator (RHI) and Plan Position Indicator (PPI) scans.

Throughout this period, the X-band radar continuously pointed at zenith. The overall scanning strategy is illustrated in Figure 2.

2.1.1 Zenith observations

The radar data were processed in three main steps, following the methodology described in von Terzi et al. (2022).

First, all radar measurements were interpolated to a common reference time-height grid with a resolution of 4 seconds in time and 36 meters in height, using a nearest-neighbor approach with a tolerance of ±17 meters in range and ±2 seconds in time. Second, the radar reflectivity (Ze) from the X-band radar was evaluated using the reflectivity calculated from a PARSIVEL optical disdrometer as a reference. Third, reflectivity values were corrected for attenuation effects, and dual-wavelength ratios (DWRs) were adjusted relative to the calibrated X-band radar.

https://doi.org/10.5194/egusphere-2026-3865
Preprint. Discussion started: 7 August 2026

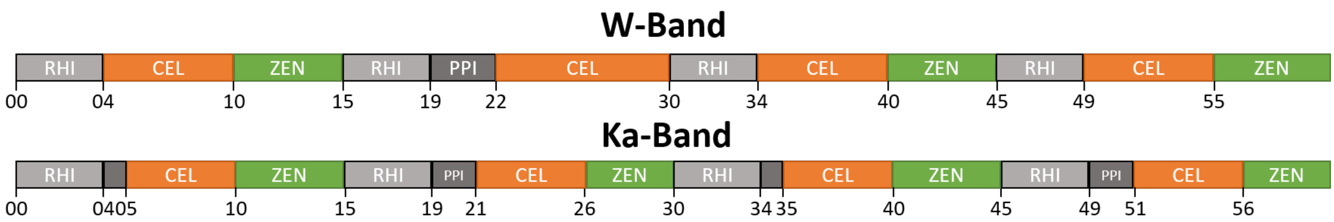

Figure 2. Scanning pattern of the W-Band (top row) and Ka-Band (bottom row) radars. This scanning pattern was performed every hour during the TRIPEx-scan campaign. Each coloured box represents one scanning pattern, the width of the box is correlated to the time length during which the scan was performed. Light grey colours indicate RHI scans, dark grey colours PPI scans, the for this analysis relevant observations at constant 30° elevation (CEL) and constant 90° elevation (ZEN) are indicated in orange and green respectively. The numbers on the x-axis indicate the start time of the scanning pattern in minutes.

As detailed in von Terzi et al. (2022), the Ze calibration was evaluated using drop size distributions (DSDs) obtained from the PARSIVEL disdrometer (Löffler-Mang and Joss, 2000). Five rain events were selected for this evaluation (see Figures A1,A2), chosen to ensure reflectivities at X-band remained below 25 dBZ while the rain intensity was sufficient for reliable DSD measurements. The expected Ze values were computed from the PARSIVEL DSDs using the T-matrix method (Mishchenko et al., 2004). These modelled reflectivities were then compared to the radar-observed Ze values at 400 m above ground level. The calibration offset was determined as the median difference between the two. Calibration was performed only for the X-band radar, as it provided continuous zenith observations. The Ka- and W-band radar reflectivities were later adjusted relative to the X-band, making a separate direct calibration unnecessary. The estimated offset for the X-band radar was 0.5 dB, with no significant drift observed over the course of the campaign.

The attenuation correction followed the procedure outlined in von Terzi et al. (2022) and Dias Neto et al. (2019). First, gaseous attenuation due to N_2, O_2, and water vapour was calculated for all radar frequencies using PAMTRA (Mech et al., 2020). Atmospheric profiles of temperature, pressure, and humidity were obtained from the ECMWF IFS model via CloudNet. Estimating attenuation due to hydrometeors is more complex, as key properties, such as particle size distribution, shape, and composition, are not directly measured. Following the approach of Hogan et al. (2000), and as applied in Tridon and Battaglia (2015) and Dias Neto et al. (2019), it was assumed that ice particles near cloud top are sufficiently small to act as Rayleigh scatterers. Under this assumption, Ze values from different radar frequencies should be equal at cloud top, and any deviation can be attributed to attenuation or miscalibration. To estimate the path-integrated attenuation and radar calibration offsets, Ze values at cloud top from the X-, Ka-, and W-band radars were compared. Given the minimal attenuation expected at X-band, the Ka- and W-band measurements were adjusted relative to the X-band reflectivity. To identify suitable regions for this comparison, dual-wavelength ratios $\mathrm{DWR}_{\mathrm{XKa}}$ and $\mathrm{DWR}_{\mathrm{XW}}$ were plotted against X-band Ze. Thresholds of $-35 < Ze_X < -5$ dBz for $\mathrm{DWR}_{\mathrm{XKa}}$, and $-35 < Ze_X < -10$ dBz for $\mathrm{DWR}_{\mathrm{XW}}$, were found to correspond to regions where Rayleigh scattering can be assumed. These regions were further restricted to lie at least 1 km above the melting layer to avoid contamination by partially melted hydrometeors. Within these selected cloud regions, calibration and attenuation offsets were computed over 30-minute

https://doi.org/10.5194/egusphere-2026-3865
Preprint. Discussion started: 7 August 2026

intervals. Only time windows with at least 300 Ze pairs and a correlation greater than 0.7 between X-band and Ka-/W-band reflectivities were included in the analysis.

2.1.2 Slanted observations

For the slant observations at a 30° elevation angle, the radar range coordinates were projected onto height above ground level. This projection results in a maximum horizontal separation of 13.86 km between zenith and slant observations at the maximum measurement height of 10 km von Terzi et al. (2022). To reduce noise in the estimation of specific differential phase shift (KDP), the differential phase shift (Φ_{DP}) was smoothed using a moving average over 30 time steps (equivalent to 2 minutes) and 5 range gates (equivalent to 180 m). The polarimetric W-band radar also provided spectrally resolved differential reflectivity (ZDR), referred to as sZDR. Because ZDR is primarily influenced by the particles contributing most to the total reflectivity (Ze), we define the maximum value within the spectrally resolved ZDR as $\mathrm{sZDR_{max}}$. This metric enables the analysis of the ZDR associated with the most asymmetric hydrometeors.

At a 30° elevation angle, Doppler velocity measurements are significantly affected by horizontal air motion, which can lead to velocity aliasing. To mitigate this, we apply a dealiasing procedure by rotating the Doppler velocity matrix until no signal appears in the velocity bin closest to ± the Nyquist velocity. Additionally, because horizontal air motion masks the fall velocity of hydrometeors, we shift the Doppler spectra at each range gate such that the slowest velocity bin is centred at 0 m/s. This adjustment simplifies the interpretation of sZDR.

The quality of polarimetric measurements is highly dependent on the signal-to-noise ratio (SNR). Therefore, our analysis includes only those polarimetric observations where the SNR exceeds 10 dB, either for the full signal or, in the case of spectrally resolved data, within each Doppler velocity bin.

2.2 The Monte-Carlo Lagrangian Particle Model McSnow

The Monte Carlo Lagrangian Particle Model McSnow (Brdar and Seifert, 2018) simulates the trajectories and microphysical evolution of individual ice particles, including properties such as mass, density, and aspect ratio. Particles evolve through depositional growth, aggregation, riming, secondary ice production, melting, and warm-rain processes (Brdar and Seifert, 2018; Bringi et al., 2020).

2.2.1 Habit prediction of ice crystals

Recently, McSnow was extended with a habit prediction scheme for monomer (single crystal) particles (Welss et al., 2023). This scheme predicts the primary habit (aspect ratio) based on ambient temperature and the secondary habit (density) as a function of particle size and temperature. Habit plays a critical role in determining the microphysical behaviour of ice particles. For example, the particle's cross-sectional area influences its fall velocity. Differences in fall velocity between particles strongly affect aggregation rates. Moreover, a larger cross-sectional area enhances the collision kernel, increasing the probability of collisions. Habit also affects sticking efficiency; dendritic particles, for instance, exhibit high sticking efficiency due

https://doi.org/10.5194/egusphere-2026-3865
Preprint. Discussion started: 7 August 2026

to mechanical interlocking. Note: this effect is not modelled directly in McSnow, rather, the assumed sticking efficiency has a maximum of 0.6 at -15°C based on laboratory data from Connolly et al. (2012).

The habit further influences depositional growth, in the maxwellian vapour deposition model, the particle geomtry influences the deposition rate via the capacitance, which is a function of Dmax and aspect-ratio. For example, plate-like crystals exhibit peak depositional growth near $-15\,°C$. Because an ice particle's habit reflects its formation and growth history, including nucleation conditions and the supersaturation and temperature it experiences during sedimentation,it can serve as a proxy for its growth pathway through the cloud.

In this study, we use an updated version of the inherent growth function (IGF2 from Welss et al. (2023)) to model habit evolution during depositional growth. With this function, ice crystals grow with a slight columnar, near isometric habit at temperatures below $-22\,°C$, transition to plate-like growth between $-22\,°C$ and $-10\,°C$ (with a maximum at $-15\,°C$), shift back to columnar growth between $-10\,°C$ and $-5\,°C$, and return to plate-like growth at warmer temperatures. Note that at temperatures colder than $-22\,°C$ the habit that particles can develop is not as easily defined as in warmer temperatures. Plate-like or columnar polycrystals have been frequently found (Bailey and Hallett, 2009). Particles can develop branches (for plates) or undergo hollowing (for columns), effectively reducing their density. While for plates the reduction in density is limited to maximum Dimension (D$-$max) exceeding 200μm, columns can hollow at all sizes.

2.2.2 Aggregation

Aggregate snowflake geometry is represented using a stochastic parametrization recently implemented in McSnow and explained in detail in Seifert et al. (2026). Instead of prescribing deterministic particle properties, key geometric quantities such as maximum dimension, aspect ratio, and area ratio are sampled from joint probability distributions derived from a large dataset of simulated aggregates generated with a detailed geometric aggregation model. The parametrization further accounts for mixtures of monomer habits through a continuous habit metric, enabling interpolation between aggregates composed of different crystal types (e.g., plates, needles, and dendrites).

Within McSnow, aggregate maximum dimension is treated as a pseudo-prognostic variable and updated during collision and depositional growth, while aspect ratio and related geometric descriptors remain fixed during depositional growth. For computational efficiency, aggregate geometry is sampled independently at each collision event without explicit memory of parent-particle structure.

Not all collisions result in aggregation; instead, a sticking efficiency is applied following the parametrization of Connolly et al. (2012), with minor modifications. Specifically, a sticking efficiency of zero is assumed in sub-saturated conditions, while a value of one is used at temperatures warmer than $-3\,°C$. This is supported by evidence that aggregation becomes highly efficient near the melting layer, likely due to the formation of a quasi-liquid layer on ice particle surfaces, which enhances sticking (Dias Neto et al., 2019; Slater and Michaelides, 2019).

https://doi.org/10.5194/egusphere-2026-3865
Preprint. Discussion started: 7 August 2026

2.2.3 Collisional fragmentation

We implemented a new fragmentation parametrization in McSnow based on laboratory studies by Grzegorczyk et al. (2023); Takahashi (1993). Fragmentation is restricted to the temperature range between $-18\,°\mathrm{C}$ and $-12\,°\mathrm{C}$, peaking at $-15\,°\mathrm{C}$, where fragmentation activity is known to be highest (Takahashi, 1993).

In the current study, we investigate fragmentation of unrimed snowflakes in a regime with low collision kinetic energy (CKE). This low-CKE regime is largely unexplored by laboratory experiments which have focused on collisions of snowflakes with high density particles, such as Graupel. Therefore we introduce here a simple fragmentation scheme with a CKE threshold of 10^{-9} J. This threshold was chosen because, according to Grzegorczyk et al. (2023), a CKE of approximately 10^{-9} J typically produces one fragment per collision. This fragmentation scheme can be understood as an approximation of the Phillips et al. (2018) or Grzegorczyk et al. (2023) scheme in the low CKE regime. To maintain flexibility, the number of fragments is determined by an input parameter N_f and a temperature-dependent scaling function a_T, with a maximum in the DGZ following Phillips et al. (2018), where $a_T = 0$ at $-18\,°\mathrm{C}$ and $-12\,°\mathrm{C}$ and $a_T = 1$ at $-15\,°\mathrm{C}$ and linear interpolation in between. Thus, the total number of fragments per collision is given by $N = N_f \cdot a_T$, constrained by the available mass of the colliding particles to ensure mass conservation.

Fragment sizes are sampled from a particle size distribution (PSD) based on Grzegorczyk et al. (2023), with a modal diameter of 75μm. Fragments are assumed to be plate-like, and their aspect ratios are computed using the size–aspect-ratio relationship for plates described in Pruppacher and Klett (1997). Once formed, fragments can continue to grow through deposition and aggregation.

2.3 Radar forward operator McRadar designed for McSnow output

We use a radar forward operator to make the model output directly comparable to radar observations. The output of a super-particle model is particularly challenging for forward operators because microphysical properties such as size, shape, mass, and composition must be accurately known and the corresponding scattering function has to be estimated as accurately as possible. A particular difficulty arises from the wide range of possible ice particle shapes. As a result, many modelling studies simplify the problem by assuming only one or a few representative shapes. In contrast, McSnow predicts a broad spectrum of ice crystal habits, which necessitates forward simulations that account for this variability. To enable this, a comprehensive ice particle scattering database was developed by von Terzi et al. (2026) and Seifert et al. (2026), containing the scattering properties of 3,080 individual ice crystals and approximately 10 million aggregates. These properties were calculated using the discrete dipole approximation (DDA), which allows for detailed modelling of non-spherical particles. The forward operator McRadar described in von Terzi et al. (2026) is applied to the McSnow output. For this study, we are using the changes described in Seifert et al. (2026). Namely, the aggregates are selected based on the mass, size, habit and orientation from the database of 10 million aggregates using a k-dimensional tree (in this case, k=4, equal to the number of variables used for selection). The monomers are selected from the monomer database based on the mass, size, aspect ratio and orientation using the ten nearest neighbours, and weighing with the inverse distance of each neighbour. The specific radar parameters of the

https://doi.org/10.5194/egusphere-2026-3865
Preprint. Discussion started: 7 August 2026

TRIPEx-scan campaign (i.e. beam width of the radars, number of FFTs, Nyquvist range and noise level) are used to simulate the radar variables. We applied the eddy dissipation rate retrieval of Chellini and Kneifel (2024), which revealed an average eddy dissipation rate of 10^{-6} m^2s^{-3} in the ice phase. This eddy dissipation rate was used to calculate the broadening of the Doppler spectrum due to turbulence. Compared to similar clouds as investigated for example in Chellini and Kneifel (2024), this eddy dissipation rate lies within the lowest quantile.

3 A Case Study Exhibiting Typical DGZ Signatures

As McSnow is a Lagrangian particle model, it would be computationally expensive to run an ensemble of simulations, as for example in the study of Karrer et al. (2021), to compare directly with our radar statistics. Therefore, in this study, we chose to test different scenarios of possible ice microphysical processes (IMP) in the dendritic growth zone (DGZ) within a case study framework. To this end, a single case from the TRIPEx-scan campaign was selected, which exhibits characteristic radar signatures associated with the DGZ. During this event, a high number of 8 radiosondes were launched within a time period of 14 h, providing valuable atmospheric information necessary for accurate modelling of depositional growth and related processes.

On 6th February 2022, a frontal system passed over JOYCE-CF. From 03:00 UTC onwards, rain reached the ground and gradually increased in intensity until 16:00 UTC, resulting in a total accumulated precipitation of 13.4 mm, as measured by a Parsivel disdrometer. Throughout most of the day, the mean Doppler velocity (MDV) above the melting layer in Figure 3b is predominantly around -1 m s^{-1}, indicating the presence of mostly unrimed snow.

This case study reveals similar radar signatures in the DGZ to those found in the statistical analysis presented in Figure 1 and in previous literature (von Terzi et al., 2022). DWR (Figure 3c,d) and Ze (Figure 3a) generally increase towards warmer temperatures throughout the day, indicating growth through aggregation. Notably, during the night and early morning, DWR increases first within the DGZ, likely due to enhanced aggregation efficiency at temperatures near $-15\,°C$ associated with dendritic growth. Enhanced $sZDR_{max}$ values reaching up to 3.5 dB around $-10\,°C$ provide further evidence of plate-like particle growth.

In the early morning, enhanced KDP is observed below the $sZDR_{max}$ maximum, possibly hinting at secondary ice production (SIP) potentially increasing the number concentration of plate-like particles. After 10:30 UTC, large patches of enhanced KDP are observed without corresponding increases in $sZDR_{max}$. The exact cause of these enhanced KDP signals is unclear. For example, Kötsche et al. (2025) demonstrated the complexity of interpreting KDP in snow, as similar KDP values can be produced by largely varying number concentration and particle types. In their case study, aggregates attributed to 20% of observed KDP. Similarly, Griffin et al. (2018) showed that the observed polarimetric variables ZDR and KDP largely depend on the relative contributions of isometric particles, such as aggregates or isometric crystals, and asymmetric particles, such as dendritic or plate-like crystals. Large KDP, in the absence of enhanced ZDR was attributed to large concentrations of isometric particles, while enhanced KDP and ZDR might be caused by dendritic or plate-like particles. In our case study, co-located or slightly lower altitude enhancements in DWR suggest that aggregates could be responsible for the enhanced KDP. Notably,

https://doi.org/10.5194/egusphere-2026-3865
Preprint. Discussion started: 7 August 2026

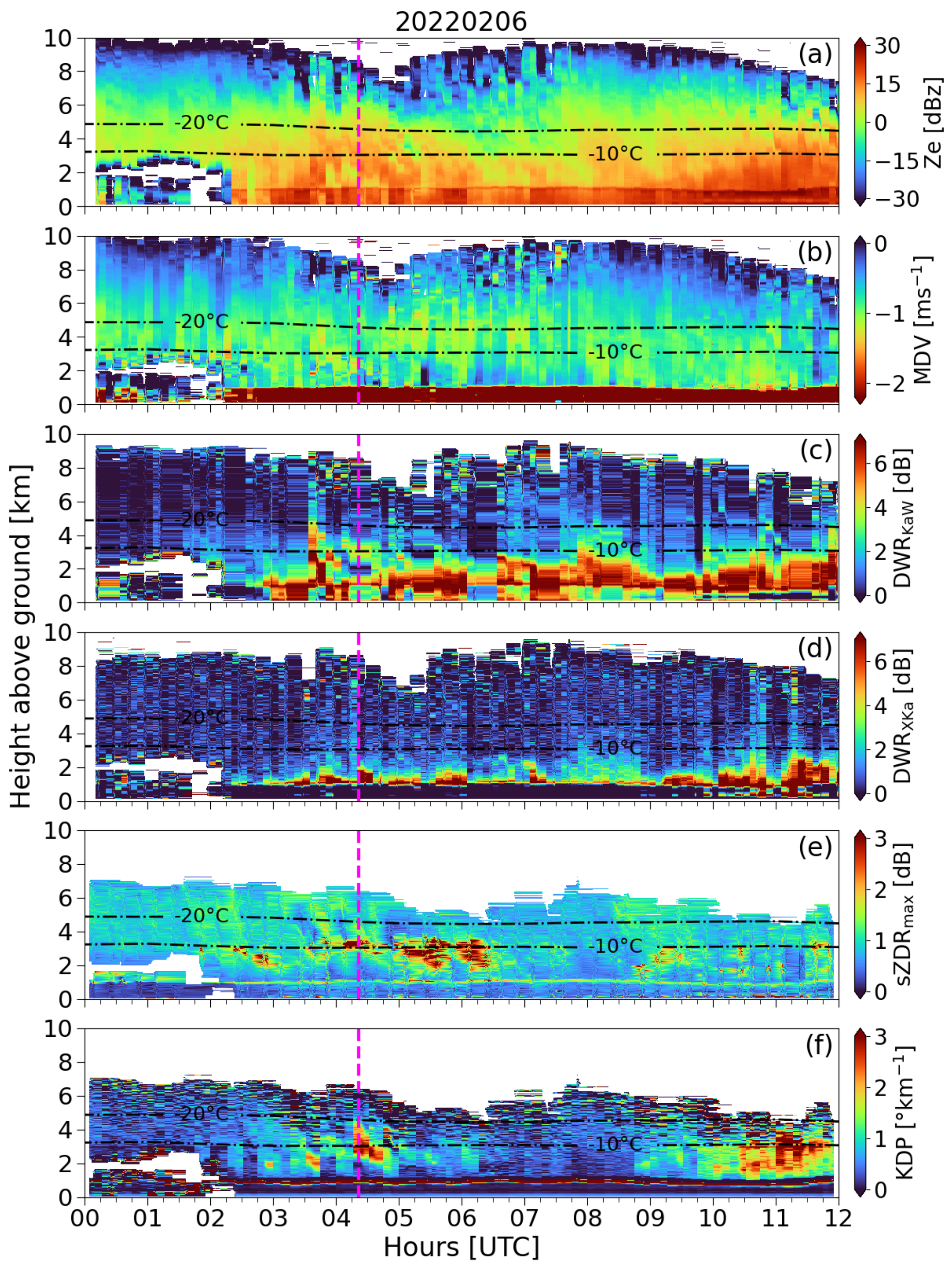

Figure 3. Time-height plots of radar moments collected on 6th February 2022. The vertical cyan line indicates the launch time of a radiosonde, which is identical to the time investigated in more detail in Figure 4 and Section 4. Panels (a) and (b) show Ze and MDV at Ka-Band and zenith elevation, panels (c) and (d) show the dual-wavelength ratios between Ka-W (c) and X-Ka (d) at zenith elevations, panels (e) and (f) show $sZDR_{max}$ and KDP at 30° elevation and W-Band. The 30° elevation observation were projected onto height above ground, as described in Section 2.1.2. For better visibility, the data were interpolated with the nearest neighbour onto a common time-height grid.

https://doi.org/10.5194/egusphere-2026-3865
Preprint. Discussion started: 7 August 2026

all polarimetric variables are used only when the signal-to-noise ratio (SNR) in both horizontal and vertical channels exceeds 10 dB.

To gain more insight into the vertical evolution of ice microphysical processes, we analyse profiles of radar moments and Doppler spectra (Figure 4) at the time of the radiosonde launch (04:21 UTC, indicated by the magenta line in Figure 3). In order to reduce high-frequency temporal fluctuations, radar profiles were averaged over 30 minutes around the launch time for, except for the Doppler spectra. Since turbulence and vertical air motion broaden Doppler spectra, long averaging times would obscure microphysical information. Therefore, Doppler spectra are shown for the time step closest to the radiosonde launch.

As also indicated in the time–height plots, Figure 4 reveals that DWR begins to increase in the DGZ from approximately $-18\,^{\circ}$C, with the strongest enhancement at $-15\,^{\circ}$C and a maximum at $-11\,^{\circ}$C. At the same level, an enhancement in sZDR (as well as $\mathrm{sZDR}_{\max}$) is observed, indicating that plate-like crystals are growing in the same region where aggregates reach their largest size. A secondary spectral mode of slowly falling particles becomes apparent in sZe, possibly contributing to a slight slowdown in MDV. This second mode is likely composed of the same ice particles that cause the sZDR increase, as it occurs at similarly low fall velocities.

Interestingly, KDP increases nearly linearly with temperature and peaks just below the DGZ at $-9\,^{\circ}$C, indicating a general increase in number concentration and size of ice particles throughout the profile. At warmer temperatures, DWR, $\mathrm{sZDR}_{\max}$, and KDP decrease, suggesting a reduction in particle size and concentration. This decrease is likely due to reduced relative humidity, which reaches a minimum of 80% with respect to ice at $-9\,^{\circ}$C (see Figure B1).

The most widely accepted explanation for the observed radar signatures is that dendritic particles grow efficiently around $-15\,^{\circ}$C, increasing Z_{DR} and KDP. The vertical separation of the peaks in Z_{DR} and KDP, with KDP peaking at warmer temperatures, has been frequently observed (Moisseev et al., 2015; von Terzi et al., 2022). Moisseev et al. (2015) has attributed this displacement to early aggregates retaining enough asymmetry to contribute to KDP, while their reduced density causes Z_{DR} to diminish.

The origin of these dendritic particles remains unclear. Three explanations have been proposed in the literature: (1) small sedimenting particles enter the DGZ from above and grow via deposition in the favourable environment at $-15\,^{\circ}$C, enhancing Z_{DR} and KDP (e.g. Moisseev et al., 2015); (2) enhanced primary nucleation due to upward air motion (Zawadzki, 2013); or (3) secondary ice production near $-15\,^{\circ}$C increases the number concentration of plate-like particles, which then grow efficiently by deposition (e.g. Kennedy and Rutledge, 2011). All mechanisms might produce a secondary spectral mode. Fragmentation is one likely process as it is known to be active in the DGZ (Grzegorczyk et al., 2023; Takahashi et al., 1995). Once formed, dendritic particles tend to aggregate efficiently due to their branched structure, increasing $\mathrm{DWR}_{\mathrm{KaW}}$ while decreasing Z_{DR} and KDP.

Investigating IMP using radar observations is inherently challenging because the radar does not observe the processes directly, but rather their effects on the ice particle properties. However, combining polarimetric radar, Doppler spectra, and multi-frequency observations improves our ability to infer these processes. Certain aspects, such as the origin of ice particles, remain beyond the reach of remote sensing alone. A Lagrangian super-particle model, such as McSnow, combined with a radar forward operator provides a framework to test our formulated hypotheses about likely growth scenarios in the DGZ.

https://doi.org/10.5194/egusphere-2026-3865
Preprint. Discussion started: 7 August 2026

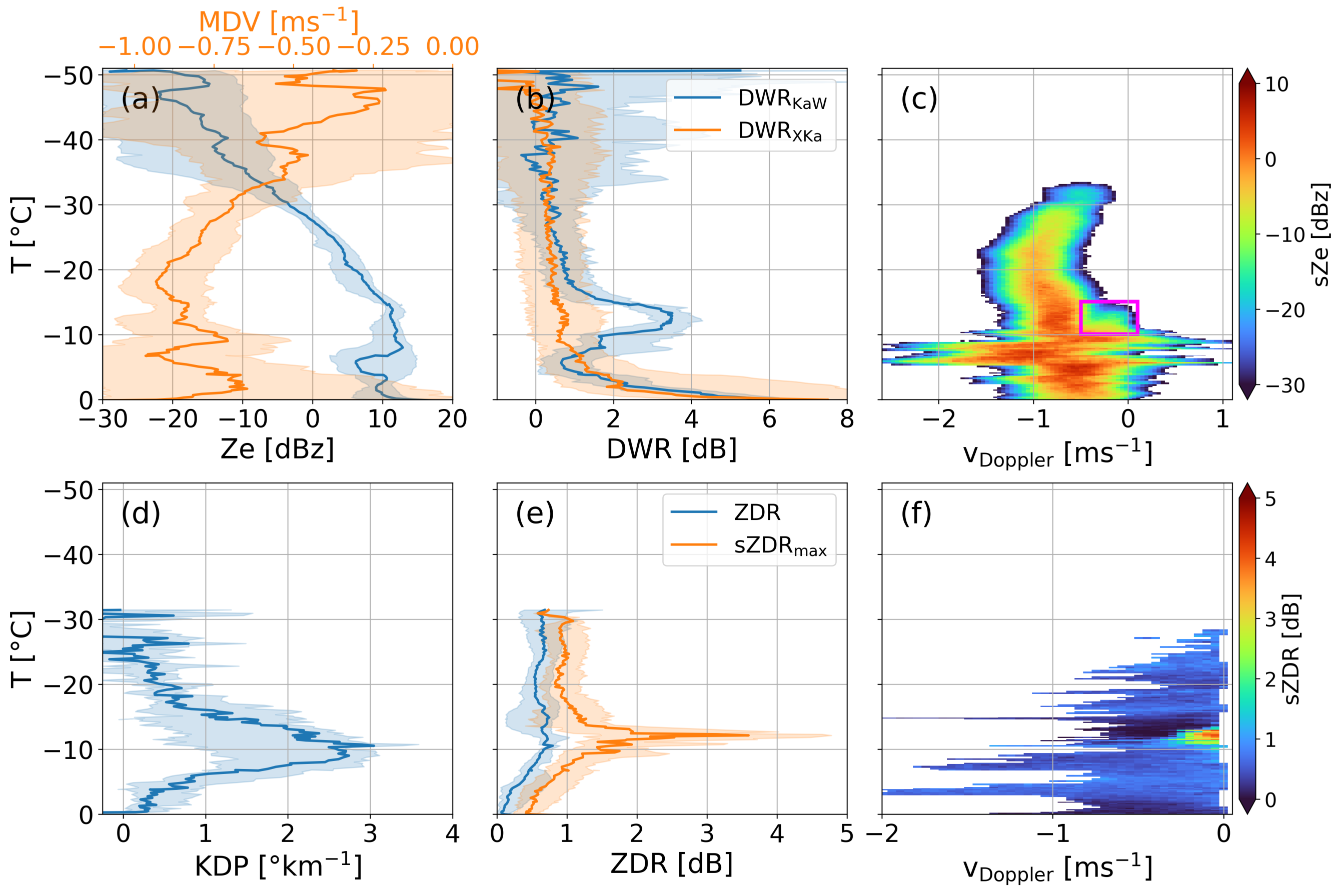

Figure 4. Radar profiles and Doppler spectra at the time of the radiosonde launch. All profiles are averaged in a 30 min window centred at the launch of the radiosonde at 04:21 UTC on 6th June 2022. To minimize spectral broadening due to a long averaging time, the Doppler spectra were selected closest to the time of radiosonde launch. The magenta rectangular in panel (c) highlights the region where a secondary, slow-falling spectral mode can be seen.

https://doi.org/10.5194/egusphere-2026-3865
Preprint. Discussion started: 7 August 2026

4 Investigating the Radar Signatures in the DGZ with McSnow

In this section, we explore how the different assumptions (hypotheses) affect the simulated radar features and evaluate which scenarios provide the best agreement with the observations and can account for the observed features.

4.1 Simulation Setup

The simulations were carried out using a 1D "shaft" model configuration. Such one-dimensional setups have been applied in several previous studies to analyze the sensitivity of microphysical quantities and radar observations to specific processes and parameters (Karrer et al., 2021; Kumjian and Ryzhkov, 2010; Seifert, 2008; Hu and Srivastava, 1995). Hu and Srivastava (1995) and later Seifert (2008) explored how raindrop evaporation and collisional breakup influence drop size distributions (DSDs), while Kumjian and Ryzhkov (2010) investigated the effect of evaporation on polarimetric radar variables. Karrer et al. (2021) used a similar framework to assess aggregation sensitivities to parameters such as the particle size distribution width or fall velocities.

The advantage of a 1D model is that it drastically reduces complexity compared to full 3D microphysical simulations. In this setup, atmospheric profiles (e.g., temperature, relative humidity) are prescribed, and feedbacks between microphysics and dynamics are neglected. This makes 1D models computationally efficient, thereby enabling sensitivity studies and supporting a process-based interpretation of the underlying processes. However, this simplification comes at the cost of realism: important features such as turbulence and vertical air motion are excluded, and the lack of feedback mechanisms may introduce biases.

To explore the hypotheses outlined in Section 3, three distinct simulations were conducted. In each simulation, we introduce a nucleation layer. In this layer, ice particles are inserted according to a prescribed nucleation rate, an aspect ratio of 1, a mean diameter of 10 μm, and a bulk ice density. As we do not have any information about the real nucleation rate for this case, we defined a nucleation rate that increases exponentially with decreasing temperature, reflecting the general trend of higher ice nucleating particle (INP) concentrations at colder temperatures (Kanji et al., 2017). The total number of nucleated particles was chosen such that the simulated radar reflectivity (Ze) profiles at temperatures colder than $-20\,^{\circ}$C match the observations reasonably well. Since the observed Ze values lie mostly above the 75th percentile of the statistical climatology in Figure 1, slight underestimations in this temperature range were deemed acceptable. The final concentration of nucleated ice particles falls within the expected range from in situ observations (Kanji et al., 2017), as shown in Figure C1.

Once initialized, particles evolve via depositional growth (with shape evolution following the scheme of Welss et al. (2023)), aggregation, and, in one scenario, fragmentation. While McSnow supports riming processes (Seifert et al., 2019), riming does not occur in these simulations because the relative humidity in the DGZ is below water saturation (see Figure B1), making the formation of supercooled liquid droplets, and thus riming, unlikely.

The three simulations are designed to test the following scenarios:

- **Simulation 1 (Sedimentation Hypothesis)**: The nucleation layer spans $-50\,^{\circ}$C to $-20\,^{\circ}$C, representing particles that nucleate above the DGZ and sediment into it. This setup allows us to investigate whether the radar signatures in the DGZ can be explained solely by particles growing as they fall into this layer.

https://doi.org/10.5194/egusphere-2026-3865
Preprint. Discussion started: 7 August 2026

- **Simulation 2 (Primary nucleation Hypothesis)**: The nucleation layer spans $-50\,^{\circ}\mathrm{C}$ to $-10\,^{\circ}\mathrm{C}$, allowing ice particles to also be initialized within the DGZ. This configuration tests the hypothesis that primary nucleation within the DGZ contributes significantly to the observed radar features.

- **Simulation 3 (Fragmentation Hypothesis)**: Identical to Simulation 1 but with collisional fragmentation enabled. This scenario explores the role of fragmentation as an additional particle generation mechanism, particularly active within the DGZ, as suggested by previous studies (Grzegorczyk et al., 2023; Takahashi et al., 1995).

Simulated radar observables from these three simulations are shown in Figure 5, and will be discussed in the following sections. Although our focus is on processes in the DGZ, we have also included the simulation results in the sublimation layer between $-9\,^{\circ}\mathrm{C}$ and $-3\,^{\circ}\mathrm{C}$ for completeness. However, due to the complex and poorly constrained processes occurring in this region, especially as sublimation likely dominates, we mark this zone in grey in Figure 5 to indicate that it is not central to the current analysis.

4.2 Simulation 1: Ice particles sedimenting into the DGZ

In Simulation 1 (Figure 5 IIa–IIf), the equivalent radar reflectivity factor Ze is generally well reproduced. As described above, Ze is used to constrain the ice nucleation rate at temperatures colder than $-20\,^{\circ}\mathrm{C}$, which partly explains the good agreement in the upper part of the profile. At warmer temperatures, the agreement remains reasonable: at $-9\,^{\circ}\mathrm{C}$, both observations and simulation reach a maximum Ze of approximately 15 dBZ.

The simulation allows a separation of the radar signal contributions from monomers and aggregates. Throughout most of the profile, Ze is dominated by ice crystals, with aggregates contributing significantly only at temperatures warmer than approximately $-10\,^{\circ}\mathrm{C}$.

In contrast to Ze, the dual-wavelength ratio $\mathrm{DWR}_{\mathrm{KaW}}$ is not as well matched. In the observations, $\mathrm{DWR}_{\mathrm{KaW}}$ increases sharply starting near $-18\,^{\circ}\mathrm{C}$ and reaches a pronounced peak of 3.5 dB at $-15\,^{\circ}\mathrm{C}$. In the simulation, however, $\mathrm{DWR}_{\mathrm{KaW}}$ only begins to increase at $-15\,^{\circ}\mathrm{C}$ and shows no distinct peak, instead continuing to increase gradually towards the melting layer, where it reaches approximately 3 dB. This discrepancy indicates that aggregation is underestimated in the simulation for this case study, pointing either to missing aggregation-enhancing processes in McSnow or to a mischaracterisation of the sticking efficiency governing aggregation.

Both the observations and the McSnow simulation exhibit a distinct slow-down of the mean Doppler velocity (MDV) near $-15\,^{\circ}\mathrm{C}$. Previous studies have attributed such slow-downs to a combination of a secondary, slow-falling Doppler spectral mode and the presence of updrafts (see for example Schrom and Kumjian, 2016; Schrom et al., 2015; Zawadzki, 2013). As McSnow does not simulate vertical air motion, updrafts cannot explain this feature. Interestingly, the simulation also does not show a separated second slower falling mode, which typically causes a slow-down at the slow-falling Doppler spectrum edge. Instead, a slow-down at the fast falling edge is seen. An examination of the microphysical properties (see Figure 6) of the particles at the fast falling edge revealed that these are columnar particles. Due to habit growth transitions from columnar to plate-like shapes within the DGZ, particle density decreases while cross-sectional area increases, resulting in reduced fall velocities. This

https://doi.org/10.5194/egusphere-2026-3865
Preprint. Discussion started: 7 August 2026

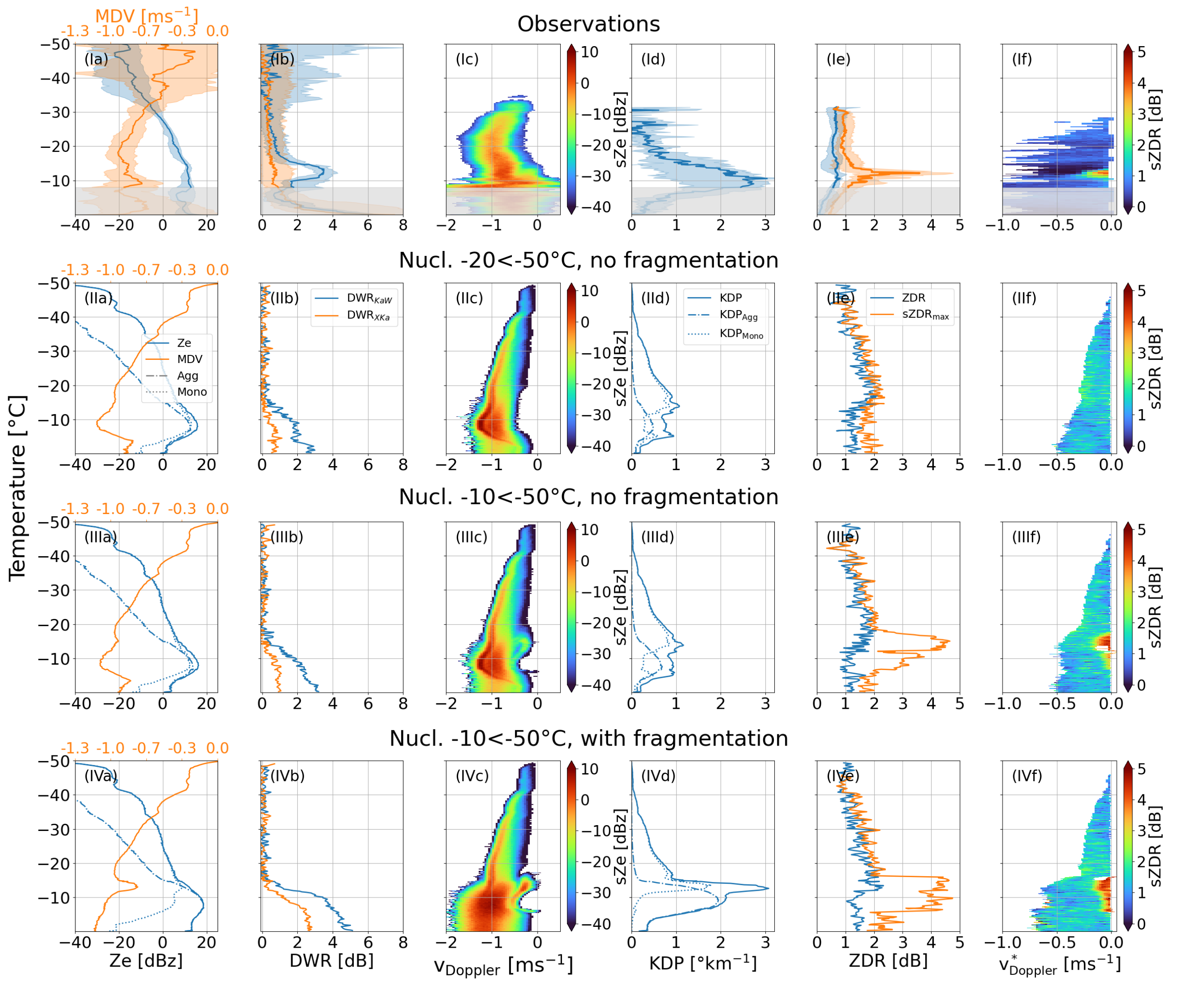

Figure 5. First row: observations, second row: McSnow simulation with primary nucleation at temperatures colder than $-20\,^{\circ}$C, third row: McSnow simulation with primary nucleation at temperatures colder than $-10\,^{\circ}$C, fourth row: McSnow simulation with primary nucleation at temperatures colder than $-20\,^{\circ}$C and fragmentation active in the DGZ. The first column shows the observed/simulated Ze and MDV at Ka-Band and 90° elevation. Second column: observed/simulated $\mathrm{DWR_{KaW}}$ and $\mathrm{DWR_{XKa}}$ at 90° elevation; third column: observed/simulated Doppler spectra at Ka-Band and 90° elevation; fourth column: KDP at W-band and 30° elevation; fifth column: ZDR and $\mathrm{sZDR_{max}}$ at W-Band and 30° elevation; sixth column: spectral ZDR (sZDR) at W-Band and 30° elevation. As in Figure 4, the colored shaded area in the first row indicates the 10th and 90th percentile of the observations within the 30 minutes averaging window. The greyed out area at temperatures warmer than $-8\,^{\circ}$C masks the part where sublimation dominates.

https://doi.org/10.5194/egusphere-2026-3865
Preprint. Discussion started: 7 August 2026

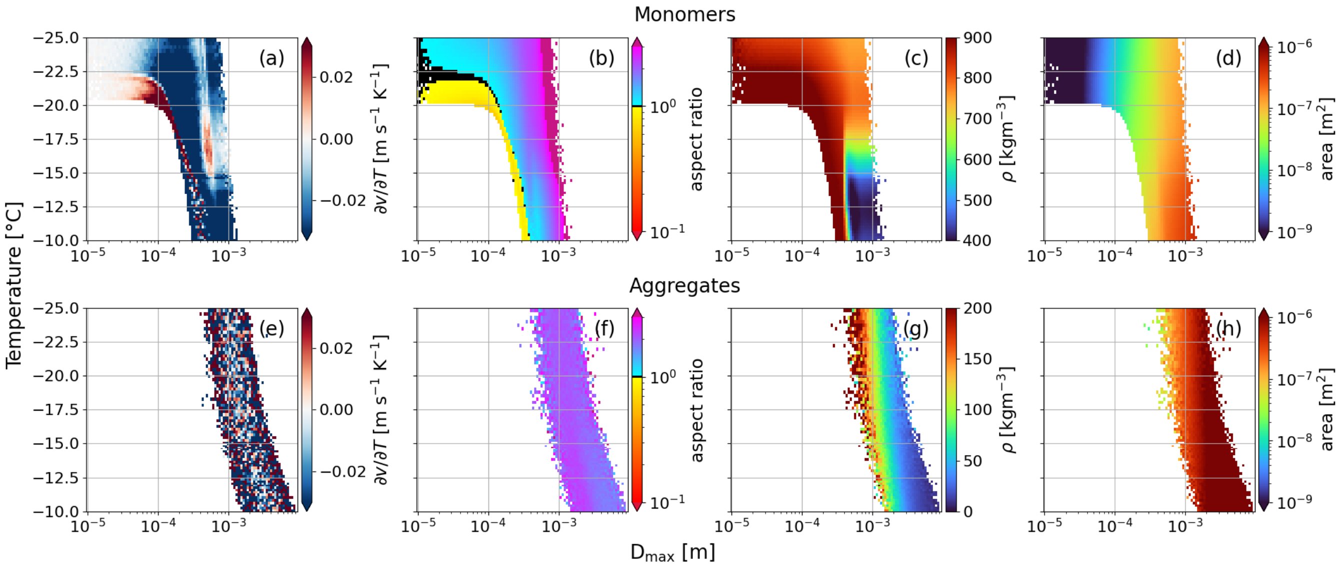

Figure 6. Microphysical properties of the ice particles of the first simulation. The properties are plotted separately for monomers (first row) and aggregates (second row). Shown are the velocity gradient with temperature (first column, positive values indicate a slow-down of fall velocity), aspect ratio (second column), the density (third column) and cross-sectional area (fourth row).

slow-down causes both the slow-down at the fast falling Doppler spectra edge and the majority of the slow-down of the MDV. The slow-down of the MDV is further strengthened by the increasing influence of aggregates, which are falling slower than the dominating columnar crystals. The increasing influence of aggregates on Ze and thus MDV further reduces MDV at -15°C.

While the non-polarimetric radar variables (Ze and MDV) are generally well reproduced, the polarimetric variables KDP and $sZDR_{max}$ are strongly underestimated. In the observations, KDP reaches a maximum of $2.7\,°\mathrm{km}^{-1}$ at $-9\,°\mathrm{C}$, whereas the simulation peaks at only $1.1\,°\mathrm{km}^{-1}$ at $-15\,°\mathrm{C}$, corresponding to an underestimation by a factor of 2.7. Similarly, the observed $sZDR_{max}$ reaches 3.7 dB at $-12\,°\mathrm{C}$, while the simulation shows no clear peak and attains values of only about 2 dB within the DGZ. During the 30-minute observation window, $sZDR_{max}$ even reaches up to 4.8 dB, implying an underestimation by a factor of 1.9–2.4 in the simulation. In addition, the simulation does not reproduce the observed enhancement of spectral ZDR on the slow-falling side of the Doppler spectrum between -13 and $-11\,°\mathrm{C}$.

Interestingly, aggregates in the simulation exhibit relatively large ZDR values: spectral ZDR on the fast-falling side is overestimated by approximately 1 dB, leading to a corresponding overestimation of ZDR and $sZDR_{max}$ throughout much of the profile. Aside from this bias, ZDR is reasonably well matched overall, consistent with the absence of a pronounced ZDR maximum in the observations due to the dominance of aggregates in the DGZ, which typically exhibit low ZDR.

The lack of pronounced polarimetric signatures in the simulated DGZ suggests that the sedimenting columnar particles have already grown to a certain size which makes a transition into plate-like habits in the DGZ rather unlikely as they would need to reach very large sizes. Instead, the dominant growth axis changes, resulting in particles with aspect ratios closer to unity

https://doi.org/10.5194/egusphere-2026-3865
Preprint. Discussion started: 7 August 2026

and consequently weaker polarimetric signals. Although McSnow's plate-like growth regime extends up to $-22\,^{\circ}$C, plate-like particles initialised at this temperature do not experience sufficiently strong growth at $-15\,^{\circ}$C. Plate-like particles sedimenting into the DGZ aggregate rapidly and largely disappear near $-15\,^{\circ}$C (not shown), further suppressing the simulated polarimetric signatures.

4.3 Simulation 2: Nucleation within the DGZ

In the second simulation (Figure 5 IIIa–IIIf), primary ice nucleation was allowed to occur across the entire temperature range from -10 to $-50\,^{\circ}$C. At temperatures colder than $-20\,^{\circ}$C, the nucleation rate was identical to that used in Simulation 1. At warmer temperatures, the nucleation rate was prescribed such that the resulting number concentration of newly nucleated particles ranged between 0.5 and 1 m^{-3}. While such ice-nucleating particle (INP) concentrations have been observed (e.g. Kanji et al. (2017), see Figure C1), they represent the upper bound of expected values.

At temperatures warmer than approximately $-25\,^{\circ}$C, ice nucleation is typically dominated by heterogeneous nucleation from the liquid phase (Kanji et al., 2017; Murray et al., 2012, and references therein). Radiosonde observations indicate that the air was persistently sub-saturated with respect to liquid water, suggesting the absence of a liquid phase during the analysed period. Consequently, significant primary nucleation within the DGZ is not expected in this specific case study, even when accounting for potential small-scale humidity fluctuations that are not resolved by the radiosonde. A radiosonde launched at 03:02:12 UTC did indicate saturation with respect to liquid water near $-15\,^{\circ}$C, implying that primary nucleation may have occurred earlier. Given the high likelihood that little or no primary nucleation occurred during the analysed period, the main purpose of this simulation is not to reproduce the specific case in detail, but rather to assess the potential impact of primary nucleation in this temperature regime on radar signatures. This allows us to evaluate whether primary nucleation within the DGZ could, in principle, explain the observed radar features in other situations. To maximise the potential influence of nucleation, a comparatively high number of nucleated particles was therefore prescribed, consistent with the upper-range INP concentrations reported by Kanji et al. (2017).

In terms of radar variables, the simulated Ze profile closely resembles that of Simulation 1. Similarly, the dual-wavelength ratios exhibit comparable behaviour, although with a slightly stronger increase towards the melting layer. While the total particle number concentration within the DGZ does not increase substantially, aggregation is enhanced. This is most likely caused by a broader particle size distribution (PSD), as the DGZ now contains a population of small, newly nucleated ice crystals that efficiently collide with larger sedimenting particles. The broader PSD is reflected in a widening of the Doppler spectrum.

A notable difference compared to Simulation 1 is the emergence of a distinct secondary spectral mode at Doppler velocities between approximately -0.25 and -0.5 m s^{-1}. This mode is populated by newly formed, plate-like ice crystals originating within the DGZ. The appearance of this slow-falling mode coincides with a pronounced peak in $sZDR_{max}$, which reaches values of up to 4.5 dB at $-15\,^{\circ}$C. The magnitude of this peak is comparable to the observed $sZDR_{max}$, indicating that the simulated particle shapes and orientations resemble those inferred from the measurements.

https://doi.org/10.5194/egusphere-2026-3865
Preprint. Discussion started: 7 August 2026

In contrast, KDP behaves very similarly to Simulation 1, with no notable enhancement resulting from the introduction of newly nucleated particles. This indicates that the additional ice crystals within the DGZ do not significantly influence KDP. Although the $sZDR_{max}$ peak is strong, it should be noted that only a small number of highly aspherical particles is required. In this simulation, particles with aspect ratios smaller than 0.07 dominate the enhancements in sZDR and spectral Ze, owing to their large sizes and extreme shapes. These particles reach a maximum concentration of approximately 0.1 m^{-3} at $-15\,°C$. While this concentration is sufficient to raise sZDR above the noise level and generate a pronounced $sZDR_{max}$ peak, it is too low to produce a detectable increase in KDP, which depends primarily on the number concentration of small, asymmetric ice crystals.

Overall, this second simulation reproduces several key observed features that were absent in Simulation 1, including a slow-falling Doppler spectral mode and a pronounced $sZDR_{max}$ peak. However, both $\mathrm{DWR_{KaW}}$ and KDP remain underestimated. The comparison between the two simulations suggests that the presence of ice particles originating within the DGZ is necessary to reproduce the observed polarimetric and spectral features, but that their simulated concentrations remain too low to substantially impact KDP and dual-wavelength ratios, even though the simulation represents the upper bound of expected primary nucleation. This hints at additional processes, such as secondary ice production, that are likely required to explain the full set of observed DGZ radar signatures.

4.4 Simulation 3: Collisional Fragmentation within the DGZ

In the third simulation, we test the hypothesis that the polarimetric signatures are primarily caused by secondary ice production, specifically collisional fragmentation. The simulation setup is identical to that in Simulation 1, with nucleation between $-20\,°C$ and $-50\,°C$, but extended to include the collisional fragmentation parameterization described in Section 2.2. In this scheme, ice fragments are produced when ice particles collide within the DGZ, with a peak number of fragments produced at $-15\,°C$.

When collisional fragmentation is included, all radar observables are altered relative to the two previous simulations. Ze shows a substantial increase around $-15\,°C$, reaching a maximum of 19.5 dBZ at $-9\,°C$. Aggregates are now dominating Ze at temperatures warmer than $-15\,°C$. Consequently, $\mathrm{DWR_{KaW}}$ increases more strongly than in previous simulations. The initial fast increase in the DGZ is followed by a slower increase towards the melting layer, finally reaching a maximum of 4.9 dB. The magnitude of $\mathrm{DWR_{KaW}}$ is now more similar to the observations. $\mathrm{DWR_{XKa}}$ also increases, reaching a maximum of 2.5 dB at the melting layer. These enhancements in Ze and DWR suggest that fragments generated in the DGZ significantly drive aggregation, increasing both the size and number of aggregates. This is corroborated by looking at the total number concentration of aggregates in the simulation compared to the other simulations (Figure 7). While the concentration of aggregates in Simulation 1 and 2 is small (400 and 560 m^{-3} respectively), the concentration reaches a peak of 2810 m^{-3} aggregates at $-12.5\,°C$ in Simulation 3.

A distinct slow-falling mode appears in the Doppler spectrum at $-15\,°C$ with spectral Ze values of approximately -5 to -15 dBZ, matching observations. This slow-falling mode is now populated by the fragments produced during collisions. It produces the largest MDV slow-down found in all three simulations.

https://doi.org/10.5194/egusphere-2026-3865
Preprint. Discussion started: 7 August 2026

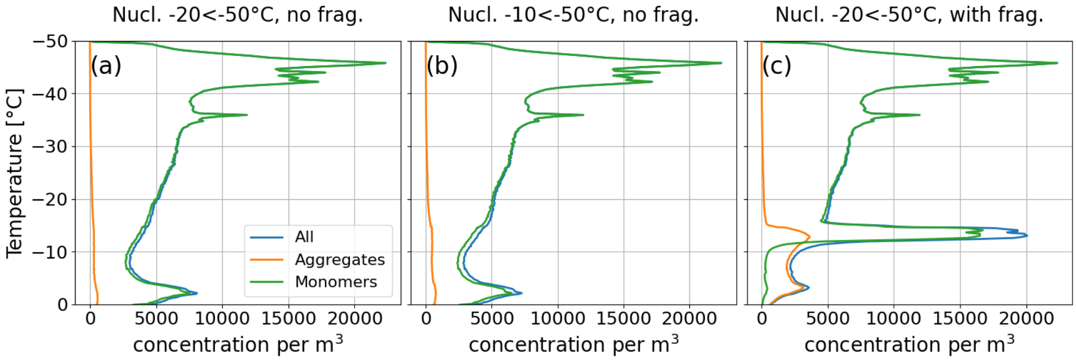

Figure 7. Number concentration of ice particles in simulations 1 (first panel), 2 (second panel) and 3 (third panel). Shown are the total number concentration (blue), the concentration of monomers (green) and the concentration of aggregates (orange).

The fragments populating the secondary, slow-falling mode, also strongly enhance $sZDR_{max}$, causing a pronounced peak within the DGZ. $sZDR_{max}$ starts increasing at $-18\,°C$, peaks at 4.5 dB near $-15\,°C$, stays continuously enhanced before sublimation eliminates plate-like monomers and $sZDR_{max}$ drops to 2.5 dB at $-8\,°C$. This maximum closely matches observations in magnitude. However, $sZDR_{max}$ stays enhanced over a deeper layer compared to the observations, which show a more rapid decrease. This might be caused by a turbulent layer at -12°C, indicated by the broader Doppler spectrum and high temporal variability of MDV at this height (not shown). Turbulence broadens the Doppler spectrum, reducing signal-to-noise ratio (SNR), particularly at the spectral edges where large $sZDR_{max}$ values occur. Consequently, even if high-$sZDR_{max}$ particles are present, they may not be detectable due to reduced SNR. Furthermore, turbulence could mix particles with varying aspect ratios into the same Doppler bin, diminishing the apparent $sZDR_{max}$. This reduction due to turbulence is also reported by Kötsche et al. (2025). In McSnow, turbulence and its effects are not included, meaning that any reduction in $sZDR_{max}$ due to turbulence is not captured. Nevertheless, the simulated evolution of particle properties with height remains physically plausible. A simulated broader $sZDR_{max}$ peak is also principally consistent with the observational statistics (Figure 1), which shows maxima occurring between $-15\,°C$ and $-11\,°C$.

The KDP obtained in this 3rd simulation shows the largest increase within the DGZ of all 3 simulations. It peaks at $2.9\,°km^{-1}$ at $-12\,°C$, before decreasing sharply. The sharp increase in KDP is primarily driven by the large number of fragments, while the peak at $-12\,°C$ is equally driven by aggregates and fragments. Towards the bottom of the DGZ, aggregation quickly reduces particle number concentration, reducing KDP. At $-9\,°C$, aggregates cause a second, smaller peak in KDP of $2\,°km^{-1}$. Sublimation reduces concentrations above $-8\,°C$, therefore also dropping KDP, which reaches $0.5\,°km^{-1}$ at the melting layer. While the magnitude in KDP is matched with the observations, the peak in KDP is at slightly colder temperatures ($-12\,°C$ in the simulation versus $-10\,°C$ in the observations).

Interestingly, the peak in $sZDR_{max}$ occurs at slightly colder temperatures than the KDP peak. This vertical displacement has been observed frequently and discussed in literature (Moisseev et al., 2015; Schrom et al., 2015; Schrom and Kumjian, 2016; von Terzi et al., 2022).

https://doi.org/10.5194/egusphere-2026-3865
Preprint. Discussion started: 7 August 2026

In this simulation, no peak in ZDR is visible because aggregates dominate the Ze. However, the altitude offset between $sZDR_{max}$ and KDP mirrors the frequently observed offset between ZDR and KDP. Simulation 2 showed that even a small concentration of plate-like crystals is sufficient to enhance $sZDR_{max}$, but not KDP. In Simulation 3, these ice crystals first appear around $-16\,^{\circ}C$ and produce a peak in $sZDR_{max}$ at $-15\,^{\circ}C$ due to minimal aspect ratios. Fragmentation significantly increases their concentration, peaking at 20 particles/m^3 at $-15\,^{\circ}C$ and remaining elevated until $-12.5\,^{\circ}C$. The KDP peak, however, occurs at $-12\,^{\circ}C$, when the concentration of plate-like particles has begun to decrease. From Figure 5IVd it can be seen that aggregates start to contribute substantially to KDP at $-15\,^{\circ}C$, and total KDP becomes a superposition of contributions from both crystals and aggregates, peaking at $-12\,^{\circ}C$. Thus, aggregation shifts the KDP peak towards warmer temperatures.

In summary, including collisional fragmentation within the DGZ results in simulated radar variables that more closely match the observations. Fragmentation leads especially to more realistic enhancements in KDP and $sZDR_{max}$, and even replicates the observed vertical offset between their peaks. Although Ze increases more than observed, such values (e.g. $Z_e \sim 20$ dBZ) are commonly recorded and not implausible.

5 Conclusions

In this study, we analyse characteristic polarimetric and multi-frequency radar signatures associated with the dendritic growth zone (DGZ). These signatures consistently include a co-occurring increase in dual-wavelength ratio (DWR), enhanced KDP and $sZDR_{max}$, the emergence of a secondary mode in the Doppler spectra, and a pronounced reduction in mean Doppler velocity around temperatures near $-15,^{\circ}$ C. At warmer temperatures, DWR typically continues to increase, while KDP and $sZDR_{max}$ decrease, indicating a transition toward aggregation-dominated conditions.

To investigate the microphysical processes underlying these signatures, we combined radar observations with the Lagrangian particle-based Monte Carlo model McSnow, including an updated habit prediction scheme (Welss et al., 2023) and a newly developed fragmentation parametrization coupled to an extensive DDA database (von Terzi et al., 2026; Seifert et al., 2026). This framework was used to test which ice microphysical processes can principally reproduce the evolution of $sZDR_{max}$, KDP, DWR, and Doppler spectral characteristics in the DGZ.

The main findings can be summarized as follows:

1. Enhanced $sZDR_{max}$ requires in-situ production of plate-like or dendritic crystals near $-15\,^{\circ}C$, either through primary nucleation or secondary ice production. Ice particles sedimenting from colder levels already exhibit a distinct columnar or isometric shape. These ice particles do not grow into plate-like particles, rather, they are changing their aspect ratio towards unity. These particles do not produce pronounced ZDR_{max} signatures near -15°C. In addition, plate-like particles sedimenting into the DGZ are aggregating efficiently before reaching the -15°C, also not contributing to enhanced $sZDR_{max}$.

2. The observed KDP enhancement within the DGZ can only be reproduced in our model simulations when ice number concentrations are increased via secondary ice production, here caused by collisional fragmentation. Neither primary nucleation nor sedimentation into the layer produces sufficient KDP to match observations.

https://doi.org/10.5194/egusphere-2026-3865
Preprint. Discussion started: 7 August 2026

3. Collisional fragmentation additionally promotes aggregation by increasing the abundance of small ice fragments participating in aggregation processes, contributing substantially to KDP and reproducing values of up to approximately $2\,^{\circ}\,\mathrm{km}^{-1}$.

4. The MDV slowdown arises from combined habit changes and aggregation of columnar ice particles entering the $-15,^{\circ}\,\mathrm{C}$ layer. Columnar particles reduce their fall speed through morphological changes, namely a decrease in density and consequently an increase in cross-sectional area (which could for example be interpreted as the development of capped columns as they sediment into the plate-like growth regime), while newly formed aggregates further enhance the reduction in MDV due to their lower terminal velocities and stronger contribution to the total radar reflectivity.

These results demonstrate that the DGZ radar fingerprints are likely to arise from a combination of interacting microphysical processes, with secondary ice production and fragmentation playing a key role in reproducing the observed polarimetric and spectral signatures. While this combined observational–modelling approach improves process understanding, substantial uncertainties remain in the representation of key microphysical mechanisms, including collisional fragmentation, aggregation efficiency, and sublimation. Targeted laboratory studies such as Grzegorczyk et al. (2023) or Gautam et al. (2024), but focussing on the low CKE regime and the specific conditions within the DGZ, are therefore essential to further constrain these processes and improve their parameterisations in numerical models.

https://doi.org/10.5194/egusphere-2026-3865
Preprint. Discussion started: 7 August 2026

Appendix A: Ze calibration using PARSIVEL measured DSDs

As described in Section 2.1 the X-Band Ze was evaluated against forward simulated Zes from Parsivel DSDs. Figure A1 shows the 5 time periods chosen for this evaluation. The time periods were chosen such that the maximum Ze at X-Band did not exceed 30 dBz, the rain was present for at least 4 hours, and the melting layer was sufficiently high above the ground. The latter criterion is relevant, as the lowest few range gates of the X-Band radar are subject to near-field effects. To avoid these effects, a lowest range gate of 400 m was chosen. A minimum time period of 4 hours was chosen, as the radar and Parsivel observation volumes do not match. The radar might observe similar rain a few minutes earlier, while the rain sediments to the ground and gets advected over the observation site. Within a longer time period, it might be assumed that statistically both instruments have sampled similar rain fall. The maximum Ze of 30 dBz was chosen to avoid receiver saturation effects.

To compare radar and Parsivel observations, the tool-kit *raincoat* (https://github.com/OPTIMICe-team/raincoat), developed within the OPTIMICE group of Stefan Kneifel, was used. First, the radar time series obtained at 400 m was downsampled to the Parsivel 1 minute time grid. Second, the Parsivel observed DSDs were forward simulated using T-Matrix calculations and maximum dimension - aspect ratio relationships of Thurai et al. (2007). Then, histograms of the radar observations and Parsivel forward simulations were calculated, and the median of the entire observation period was compared. The results are shown in Figure A2. Parsivel forward simulated Ze and the X-Band observed Zes are agreeing well, with an estimated offset of 0.5 dBz.

https://doi.org/10.5194/egusphere-2026-3865
Preprint. Discussion started: 7 August 2026

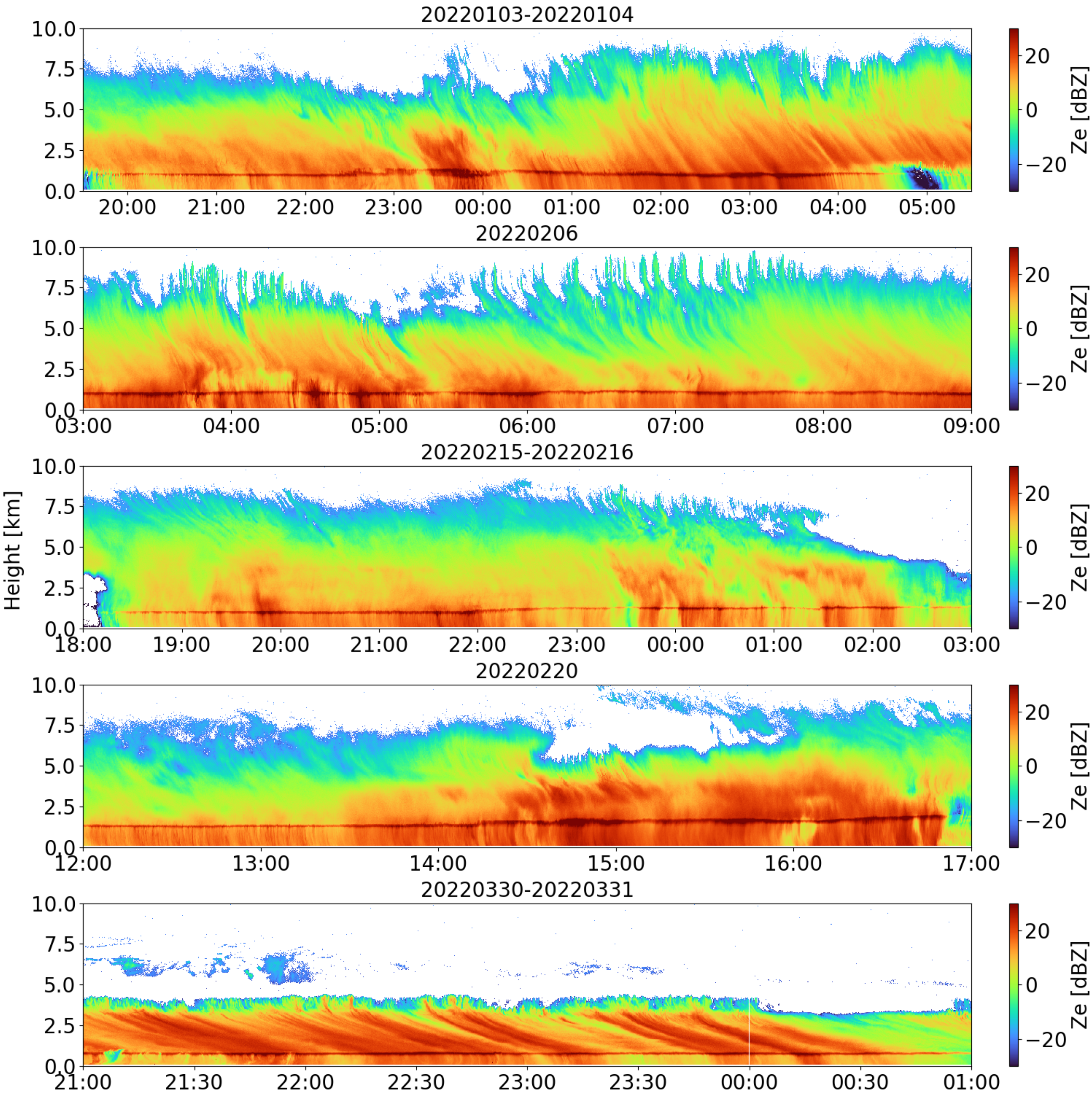

Figure A1. Time periods of Ze observations at X-Band used for the calibration with the Parsivel.

https://doi.org/10.5194/egusphere-2026-3865
Preprint. Discussion started: 7 August 2026

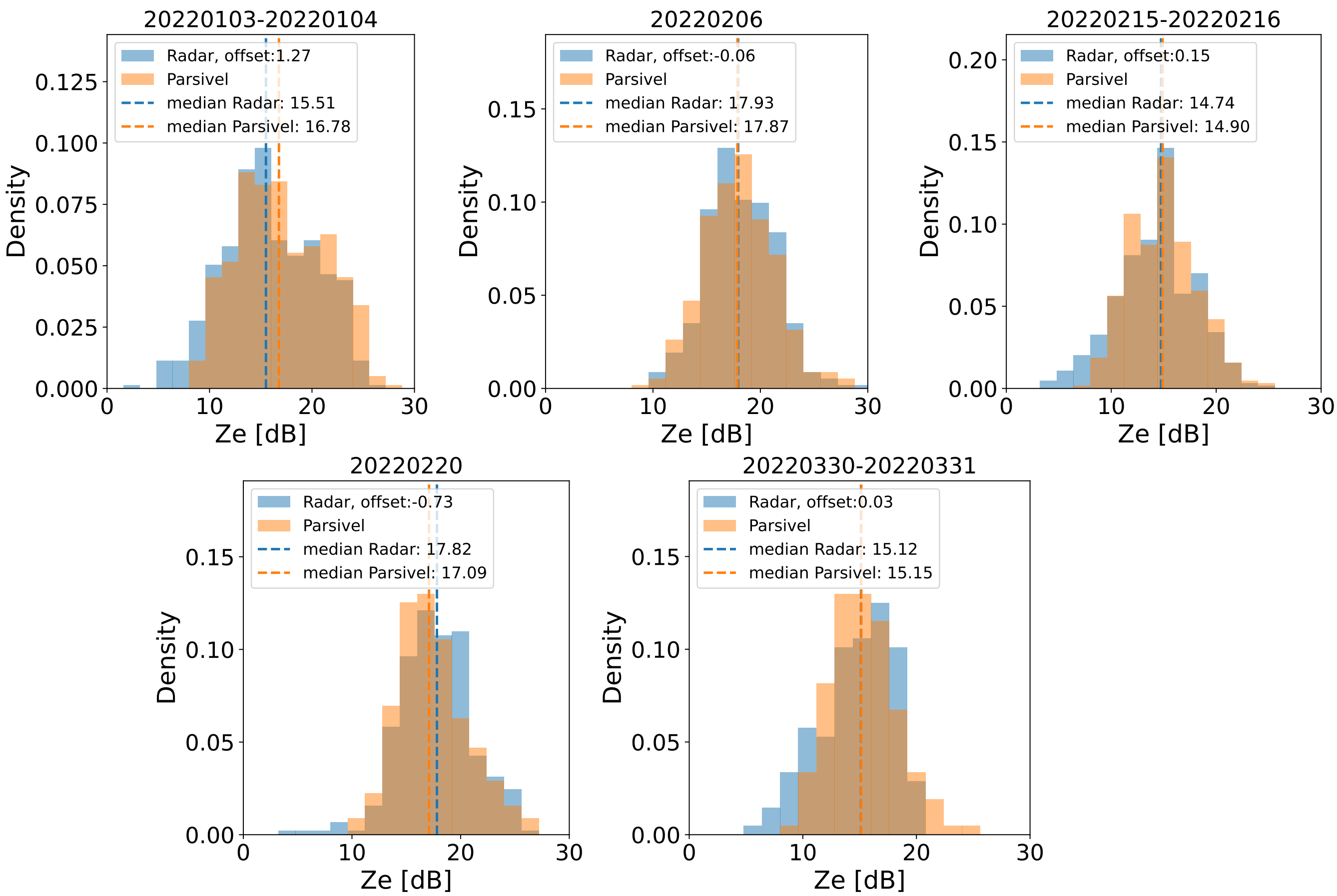

Figure A2. Histograms of Ze observed with the X-Band radar (blue) and calculated from the Parsivel (orange). Shown is also the median of the distributions and the derived offset.

https://doi.org/10.5194/egusphere-2026-3865
Preprint. Discussion started: 7 August 2026

Appendix B: Radiosonde measurements

Accurate measurements of the relative humidity and temperature are essential, as they determine the primary and secondary habits in McSnow. During the TRIPEx-scan campaign, 47 radiosondes of type RS-41 manufactured by Vaisala were launched in January and February 2022. The humidity sensor has been tested against a frostpoint hygrometer during test soundings by the manufacturer (see Vaisala Radiosonde RS41 Measurement Performance at Vaisala). This revealed an uncertainty of smaller than 4% at water saturations between 0 and 100%. The humidity sensor of these radiosondes has been calibrated before each launch.

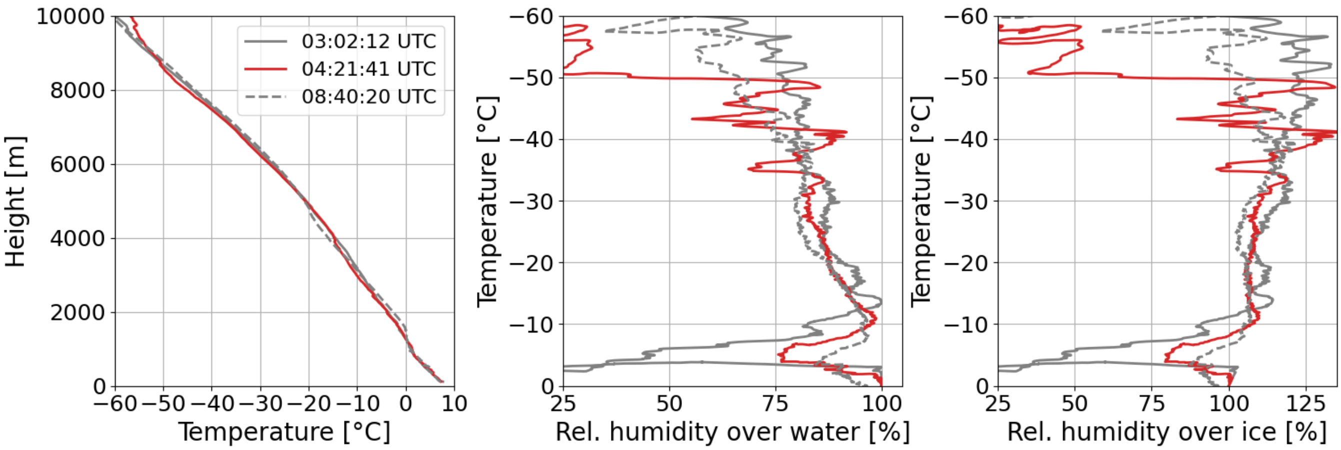

Figure B1. Radiosonde measurements at 04:21 UTC on 20220206 (red), as well as the closest radiosonde launched before and after (grey lines)

Figure B1 shows the radiosonde profile taken as atmospheric input for all McSnow simulations. As a reference, also the radiosonde launched approximately one hour earlier and four hours later are shown.

https://doi.org/10.5194/egusphere-2026-3865
Preprint. Discussion started: 7 August 2026

Appendix C: Concentration of ice particles nucleated in the McSnow simulations

Figure C1 shows the ice particle number concentration (per liter) nucleated in simulation 2. In simulations 1 and 3, nucleation was restricted to temperatures below $-20\,^{\circ}\mathrm{C}$, but the nucleated particle concentrations at those temperatures were identical across all simulations. For reference, observed INP concentrations from Kanji et al. (2017) are included in the figure. The nucleation assumptions used in our simulations fall within the observed range of INP concentrations where measurements are available. Below $-20\,^{\circ}\mathrm{C}$, the simulated nucleated particle concentrations lie near the middle of this observed range. The localized spikes of anomalously low number concentrations are an artifact of small subsaturated regions in the radiosonde profile, which locally suppress ice nucleation. At warmer temperatures, the assumed nucleation rate approaches the upper bound of observed INP concentrations, enabling an assessment of the maximum possible impact of primary ice nucleation within the dendritic growth zone (DGZ).

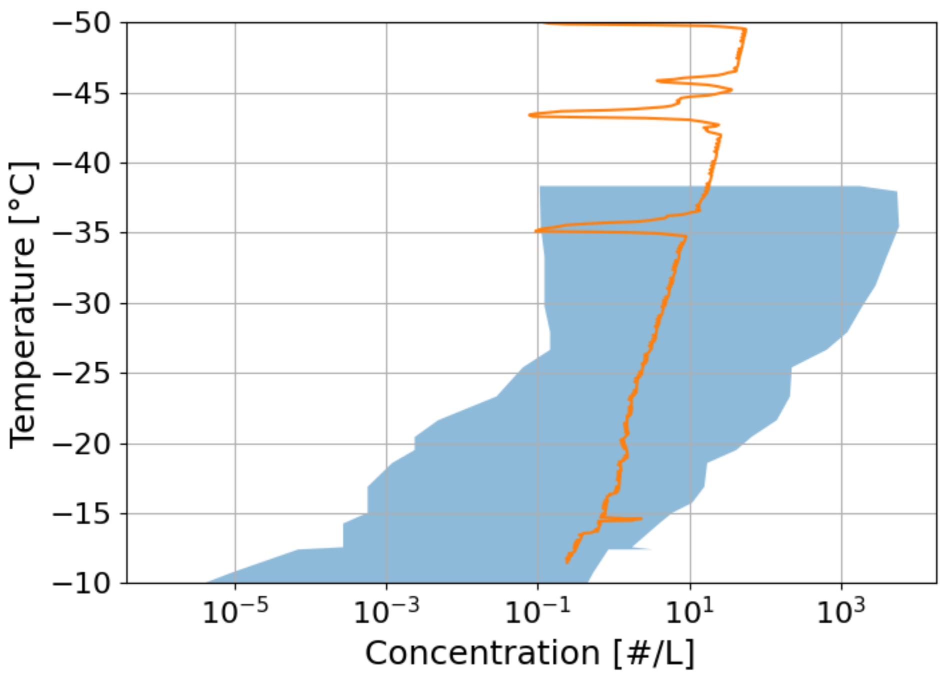

Figure C1. Number of ice particles nucleated per Liter in the McSnow simulation 2 and 3 (orange line). As a reference, the enclosure of INP concentrations as found in Kanji et al. (2017), their Figure 1-11, are shown as blue shaded area.

https://doi.org/10.5194/egusphere-2026-3865
Preprint. Discussion started: 7 August 2026

Code and data availability. The code used to perform the attenuation correction is available at https://github.com/lterzi/attenuation_correction_triple_freq. The exact version used in this publication is archived on zenodo under https://doi.org/10.5281/zenodo.20825443. *raincoat*, which was used to evaluate the X-Band Ze against Parsivel forward simulated Ze is available at https://github.com/OPTIMICe-team/raincoat. The exact version used in this publication is archived on Zenodo under https://doi.org/10.5281/zenodo.20825522. The level-2 dataset used for the statistics are archived on Zenodo under https://doi.org/10.5281/zenodo.20923427 for the tripex-pol-scan campaign and https://doi.org/10.5281/zenodo.5025636 for the tripex-pol campaign. The additional observational data needed for this paper (i.e. 5 minute averages for Figure 1 and Doppler spectra for Figures 4 and 5 are archived under https://doi.org/10.5281/zenodo.20930716. The exact version of McSnow used in this study is archived on Zenodo under https://doi.org/10.5281/zenodo.20843584. McRadar used to forward simulate the McSnow output can be found on github under https://github.com/lterzi/McRadar. The exact version used in this publication is archived on Zenodo under https://doi.org/10.5281/zenodo.17104878. The McSnow and McRadar simulation output is archive on Zenodo under https://doi.org/10.5281/zenodo.21030203. All scripts used to generate the Figures, run McSnow and McRadar are available on github at https://github.com/lterzi/Investigating_DGZ_McSnow_Obs, the exact version used in this study is archived on Zenodo under https://doi.org/10.5281/zenodo.21064015.

Author contributions. Data analysis as well as the McSnow simulations and radar forward simulations were performed by LvT. Implementation of the fragmentation parametrization into McSnow was performed by AS, CS, FJ with contributions from LvT. SK acquired funding and guided the research project. All authors contributed to the analysis of the results and preparation of the results. The AI tool ChatGPT was used to correct spelling and improve readability of the text.

Competing interests. We declare that none of the authors have competing interests.

Acknowledgements. Contributions by LvT, SK, FJ, AS, CS have been funded by the Deutsche Forschungsgemeinschaft (DFG, German REsearch Doundation) Priority Programm SPP2115 “Fusion of Radar Polarimetry and Numerical Atmospheric Modelling Towards an Improved Understanding of Cloud and Precipitation Processes” (PROM), project “Exploring the role of FRAGmentation of ice particles by combining super-partIcle modelling, Laboratory studies, and polarimEtric radar observations” (FRAGILE, project number 492234709). We would like to thank Dr. Miklós Szakall for providing his laboratory findings regarding collisional fragmentation, which was helpful to constrain the parametrization.

https://doi.org/10.5194/egusphere-2026-3865
Preprint. Discussion started: 7 August 2026

References

Andrić, J., Kumjian, M. R., Zrnić, D. S., Straka, J. M., and Melnikov, V. M.: Polarimetric Signatures above the Melting Layer in Winter Storms: An Observational and Modeling Study, Journal of Applied Meteorology and Climatology, 52, 682–700, https://doi.org/10.1175/JAMC-D-12-028.1, 2013.

Bailey, M. P. and Hallett, J.: A comprehensive habit diagram for atmospheric ice crystals: Confirmation from the laboratory, AIRS II, and other field studies, Journal of the Atmospheric Sciences, 66, 2888–2899, https://doi.org/10.1175/2009JAS2883.1, 2009.

Bechini, R., Baldini, L., and Chandrasekar, V.: Polarimetric radar observations in the ice region of precipitating clouds at C-Band and X-Band radar frequencies, Journal of Applied Meteorology and Climatology, 52, 1147–1169, https://doi.org/10.1175/JAMC-D-12-055.1, 2013.

Brdar, S. and Seifert, A.: McSnow: A Monte-Carlo Particle Model for Riming and Aggregation of Ice Particles in a Multidimensional Microphysical Phase Space, Journal of Advances in Modeling Earth Systems, 10, 187–206, https://doi.org/10.1002/2017MS001167, 2018.

Bringi, V., Seifert, A., Wu, W., Thurai, M., Huang, G.-J., and Siewert, C.: Hurricane Dorian outer rain band observations and 1D particle model simulations: A case study, Atmosphere, 11, 879, https://doi.org/10.3390/atmos11080879, 2020.

Bringi, V. N. and Chandrasekar, V.: Polarimetric Doppler Weather Radar: Principles and Applications, Cambridge University Press, https://doi.org/10.1017/CBO9780511541094, 2001.

Chellini, G. and Kneifel, S.: Turbulence as a key driver of ice aggregation and riming in Arctic low-level mixed-phase clouds, revealed by long-term cloud radar observations, Geophysical Research Letters, 51, e2023GL106 599, https://doi.org/10.1029/2023GL106599, 2024.

Connolly, P. J., Emersic, C., and Field, P. R.: A laboratory investigation into the aggregation efficiency of small ice crystals, Atmospheric Chemistry and Physics, 12, 2055–2076, https://doi.org/10.5194/acp-12-2055-2012, 2012.

Dias Neto, J., Kneifel, S., Ori, D., Trömel, S., Handwerker, J., Bohn, B., Hermes, N., Mühlbauer, K., Lenefer, M., and Simmer, C.: The TRIple-frequency and Polarimetric radar Experiment for improving process observations of winter precipitation, Earth System Science Data, 11, 845–863, https://doi.org/10.5194/essd-11-845-2019, 2019.

Draine, B. T. and Flatau, P. J.: Discrete-dipole approximation for scattering calculations, Journal of the Optical Society of America A, 11, 1491–1499, https://doi.org/10.1364/JOSAA.11.001491, 1994.

Dunnavan, E. L., Carlin, J. T., Hu, J., Bukovčić, P., Ryzhkov, A. V., McFarquhar, G. M., Finlon, J. A., Matrosov, S. Y., and Delene, D. J.: Radar retrieval evaluation and investigation of dendritic growth layer polarimetric signatures in a winter storm, Journal of Applied Meteorology and Climatology, 61, 1685–1711, https://doi.org/10.1175/JAMC-D-21-0220.1, 2022.

Field, P. R.: Bimodal ice spectra in frontal clouds, Quarterly Journal of the Royal Meteorological Society, 126, 379–392, https://doi.org/10.1002/qj.49712656302, 2000.

Field, P. R. and Heymsfield, A. J.: Importance of snow to global precipitation, Geophysical Research Letters, 42, 9512–9520, https://doi.org/10.1002/2015GL065497, 2015.

Gautam, M., Waman, D., Patade, S., Deshmukh, A., Phillips, V., Jackowicz-Korczynski, M., Paul, F. P., Smith, P., and Bansemer, A.: Fragmentation in Collisions of Snow with Graupel/Hail: New Formulation from Field Observations, Journal of the Atmospheric Sciences, 81, 2149–2164, https://doi.org/10.1175/JAS-D-23-0122.1, 2024.

Georgakaki, P., Sotiropoulou, G., Vignon, É., Billault-Roux, A.-C., Berne, A., and Nenes, A.: Secondary ice production processes in wintertime alpine mixed-phase clouds, Atmospheric Chemistry and Physics, 22, 1965–1988, https://doi.org/10.5194/acp-22-1965-2022, 2022.

Griffin, E. M., Schuur, T. J., and Ryzhkov, A. V.: A polarimetric analysis of ice microphysical processes in snow, using quasi-vertical profiles, Journal of Applied Meteorology and Climatology, 57, 31–50, https://doi.org/10.1175/JAMC-D-17-0033.1, 2018.

https://doi.org/10.5194/egusphere-2026-3865
Preprint. Discussion started: 7 August 2026

Grzegorczyk, P., Yadav, S., Zanger, F., Theis, A., Mitra, S. K., Borrmann, S., and Szakáll, M.: Fragmentation of ice particles: laboratory experiments on graupel–graupel and graupel–snowflake collisions, Atmos. Chem. Phys, 23, 13 505–13 521, https://doi.org/10.5194/acp-23-13505-2023, 2023.

Heymsfield, A. J., Schmitt, C., Chen, C. C. J., Bansemer, A., Gettelman, A., Field, P. R., and Liu, C.: Contributions of the Liquid and Ice Phases to Global Surface Precipitation: Observations and Global Climate Modeling, Journal of the Atmospheric Sciences, 77, 2629–2648, https://doi.org/10.1175/JAS-D-19-0352.1, 2020.

Hogan, R. J., Illingworth, A. J., and Sauvageot, H.: Measuring crystal size in cirrus using 35- and 94-GHz radars, Journal of Atmospheric and Oceanic Technology, 17, 27–37, https://doi.org/10.1175/1520-0426(2000)017<0027:MCSICU>2.0.CO;2, 2000.

Hu, Z. and Srivastava, R.: Evolution of raindrop size distribution by coalescence, breakup, and evaporation: Theory..., Journal of the atmospheric sciences, 52, https://doi.org/10.1175/1520-0469(1995)052<1761:EORSDB>2.0.CO;2, 1995.

Kanji, Z., Ladino, L., Wex, H., Boose, Y., Burkert-Kohn, M., Cziczo, D., and Krämer, M.: Overview of ice nucleating particles, Meteorological Monographs, 58, 1–1, https://doi.org/10.1175/AMSMONOGRAPHS-D-16-0006.1, 2017.

Karrer, M., Seifert, A., Ori, D., and Kneifel, S.: Improving the representation of aggregation in a two-moment microphysical scheme with statistics of multi-frequency Doppler radar observations, Atmospheric Chemistry and Physics, 21, 17 133–17 166, https://doi.org/10.5194/acp-21-17133-2021, 2021.

Kennedy, P. C. and Rutledge, S. A.: S-band dual-polarization radar observations of winter storms, Journal of Applied Meteorology and Climatology, 50, 844–858, https://doi.org/10.1175/2010JAMC2558.1, 2011.

Kneifel, S., von Lerber, A., Tiira, J., Moisseev, D., Kollias, P., and Leinonen, J.: Observed relations between snowfall microphysics and triple-frequency radar measurements, Journal of Geophysical Research: Atmospheres, 120, 6034–6055, https://doi.org/10.1002/2015JD023156, 2015.

Korolev, A.: Limitations of the Wegener–Bergeron–Findeisen Mechanism in the Evolution of Mixed-Phase Clouds, Journal of the Atmospheric Sciences, 64, 3372–3375, https://doi.org/10.1175/JAS4035.1, 2007.

Kötsche, A., Myagkov, A., Von Terzi, L., Maahn, M., Ettrichrätz, V., Vogl, T., Ryzhkov, A., Bukovcic, P., Ori, D., and Kalesse-Los, H.: Investigating KDP signatures inside and below the dendritic growth layer with W-band Doppler radar and in situ snowfall camera, Atmospheric Chemistry and Physics, 25, 14 045–14 070, https://doi.org/10.5194/acp-25-14045-2025, 2025.

Kumjian, M. R.: Principles and Applications of Dual-Polarization Weather Radar. Part I: Description of the Polarimetric Radar Variables, Journal of Operational Meteorology, 1, 226–242, https://doi.org/10.15191/nwajom.2013.0119, 2013.

Kumjian, M. R. and Ryzhkov, A.: The impact of evaporation on polarimetric characteristics of rain: Theoretical model and practical implications, Journal of Applied Meteorology and Climatology, 49, 1247–1267, https://doi.org/10.1175/2010JAMC2243.1, 2010.

Lamb, D. and Verlinde, J.: Physics and chemistry of clouds, Cambridge University Press, 2011.

Löffler-Mang, M. and Joss, J.: An optical disdrometer for measuring size and velocity of hydrometeors, Journal of Atmospheric and Oceanic Technology, 17, 130–139, https://doi.org/10.1175/1520-0426(2000)017<0130:AODFMS>2.0.CO;2, 2000.

Löhnert, U., Schween, J. H., Acquistapace, C., Ebell, K., Maahn, M., Barrera-Verdejo, M., Hirsikko, A., Bohn, B., Knaps, A., O'Connor, E., Simmer, C., Wahner, A., and Crewell, S.: JOYCE: Jülich Observatory for Cloud Evolution, Bulletin of the American Meteorological Society, 96, 1157–1174, https://doi.org/10.1175/BAMS-D-14-00105.1, 2015.

Matrosov, S. Y.: Radar Rrflectivity in Snowfall, IEEE Transactions on Geoscience and Remote Sensing, 30, 454–461, https://doi.org/10.1109/36.142923, 1992.

Mech, M., Maahn, M., Kneifel, S., Ori, D., Orlandi, E., Kollias, P., Schemann, V., and Crewell, S.: PAMTRA 1.0: A Passive and Active Microwave radiative TRAnsfer tool for simulating radiometer and radar measurements of the cloudy atmosphere, Geoscientific Model Development Discussions, 2020, 1–34, https://doi.org/10.5194/gmd-2019-356, 2020.

Mishchenko, M. I., Videen, G., Babenko, V. A., Khlebtsov, N. G., and Wriedt, T.: T-matrix theory of electromagnetic scattering by particles and its applications: a comprehensive reference database, J. Quant. Spectrosc. Radiat. Transfer, 88, 357–406, https://doi.org/doi:10.1016/j.jqsrt.2004.05.002, 2004.

Moisseev, D. N., Lautaportti, S., Tyynela, J., and Lim, S.: Dual-polarization radar signatures in snowstorms: Role of snowflake aggregation, Journal of Geophysical Research, 120, 12,644–12,665, https://doi.org/10.1002/2015JD023884, 2015.

Morrison, H., van Lier-Walqui, M., Fridlind, A. M., Grabowski, W. W., Harrington, J. Y., Hoose, C., Korolev, A., Kumjian, M. R., Milbrandt, J. A., Pawlowska, H., Posselt, D. J., Prat, O. P., Reimel, K. J., Shima, S.-I., van Diedenhoven, B., and Xue, L.: Confronting the Challenge of Modeling Cloud and Precipitation Microphysics, Journal of Advances in Modeling Earth Systems, 12, https://doi.org/10.1029/2019MS001689, 2020.

Mülmenstädt, J., Sourdeval, O., Delanoë, J., and Quaas, J.: Frequency of occurrence of rain from liquid-, mixed-, and ice-phase clouds derived from A-Train satellite retrievals, Geophysical Research Letters, 42, 6502–6509, https://doi.org/10.1002/2015GL064604, 2015.

Murray, B., O'sullivan, D., Atkinson, J., and Webb, M.: Ice nucleation by particles immersed in supercooled cloud droplets, Chemical Society Reviews, 41, 6519–6554, https://doi.org/10.1039/C2CS35200A, 2012.

Oue, M., Kollias, P., Ryzhkov, A., and Luke, E. P.: Toward exploring the synergy between cloud radar polarimetry and Doppler spectral analysis in deep cold precipitating systems in the Arctic, Journal of Geophysical Research: Atmospheres, 123, 2797–2815, https://doi.org/10.1002/2017JD027717, 2018.

Phillips, V. T., Patade, S., Gutierrez, J., and Bansemer, A.: Secondary ice production by fragmentation of freezing drops: Formulation and theory, Journal of the Atmospheric Sciences, 75, 3031–3070, https://doi.org/10.1175/JAS-D-17-0190.1, 2018.

Pruppacher, H. R. and Klett, J. D.: Microphysics of Clouds and Precipitation, Kluwer Academic Publishers, Dordrecht, 1997.

Schrom, R. S. and Kumjian, M. R.: Connecting microphysical processes in Colorado winter storms with vertical profiles of radar observations, Journal of Applied Meteorology and Climatology, 55, 1771–1787, https://doi.org/10.1175/JAMC-D-15-0338.1, 2016.

Schrom, R. S., Kumjian, M. R., and Lu, Y.: Polarimetric radar signatures of dendritic growth zones within Colorado winter storms, Journal of Applied Meteorology and Climatology, 54, 2365–2388, https://doi.org/10.1175/JAMC-D-15-0004.1, 2015.

Seifert, A.: On the Parameterization of Evaporation of Raindrops as Simulated by a One-Dimensional Rainshaft Model, Journal of the Atmospheric Sciences, 65, 3608 – 3619, https://doi.org/10.1175/2008JAS2586.1, 2008.

Seifert, A., Leinonen, J., Siewert, C., and Kneifel, S.: The Geometry of Rimed Aggregate Snowflakes: A Modeling Study, Journal of Advances in Modeling Earth Systems, 11, 712–731, https://doi.org/10.1029/2018MS001519, 2019.

Seifert, A., Jakub, F., Siewert, C., von Terzi, L., and Kneifel, S.: On the geometry of aggregate snowflakes, Tellus, 79, 87–110, https://doi.org/10.16993/tellus.4127, 2026.

Shupe, M. D. and Intrieri, J. M.: Cloud Radiative Forcing of the Arctic Surface: The Influence of Cloud Properties, Surface Albedo, and Solar Zenith Angle, Journal of Climate, 17, 616 – 628, https://doi.org/10.1175/1520-0442(2004)017<0616:CRFOTA>2.0.CO;2, 2004.

Slater, B. and Michaelides, A.: Surface premelting of water ice, Nature Reviews Chemistry, 3, 172–188, https://doi.org/10.1038/s41570-019-0080-8, 2019.

Takahashi, T.: High ice crystal production in winter cumuli over the Japan Sea, Geophysical Research Letters, 20, 451–454, https://doi.org/10.1029/93GL00613, 1993.

https://doi.org/10.5194/egusphere-2026-3865
Preprint. Discussion started: 7 August 2026

Takahashi, T.: Influence of Liquid Water Content and Temperature on the Form and Growth of Branched Planar Snow Crystals in a Cloud, Journal of the Atmospheric Sciences, 71, 4127–4142, https://doi.org/10.1175/JAS-D-14-0043.1, 2014.

Takahashi, T., Nagao, Y., and Kushiyama, Y.: Possible High Ice Particle Production during Graupel–Graupel Collisions, Journal of the Atmospheric Sciences, 52, 4523–4527, https://doi.org/10.1175/1520-0469(1995)052<4523:PHIPPD>2.0.CO;2, 1995.

Thompson, E. J., Rutledge, S. A., Dolan, B., Chandrasekar, V., and Cheong, B. L.: A dual-polarization radar hydrometeor classification algorithm for winter precipitation, Journal of Atmospheric and Oceanic Technology, 31, 1457–1481, https://doi.org/10.1175/JTECH-D-13-00119.1, 2014.

Thurai, M., Huang, G. J., Bringi, V. N., Randeu, W. L., and Schönhuber, M.: Drop shapes, model comparisons, and calculations of polarimetric radar parameters in rain, Journal of Atmospheric and Oceanic Technology, 24, 1019–1032, https://doi.org/10.1175/JTECH2051.1, 2007.

Tridon, F. and Battaglia, A.: Dual-frequency radar Doppler spectral retrieval of rain drop size distributions and entangled dynamics variables, Journal of Geophysical Research: Atmospheres, 120, 5585–5601, https://doi.org/10.1002/2014JD023023, 2015.

Vaisala: Vaisala Radiosonde RS41 Measurement Performance, White Paper B211356EN-A, Vaisala, https://www.vaisala.com/sites/default/files/documents/White%20paper%20RS41%20Performance%20B211356EN-A.pdf, accessed: 2026-06-24.

von Terzi, L., Dias Neto, J., Ori, D., Myagkov, A., and Kneifel, S.: Ice microphysical processes in the dendritic growth layer: a statistical analysis combining multi-frequency and polarimetric Doppler cloud radar observations, Atmospheric Chemistry and Physics, 22, 11 795–11 821, https://doi.org/10.5194/acp-22-11795-2022, 2022.

von Terzi, L., Ori, D., and Kneifel, S.: A Microwave Scattering Database of Oriented Ice and Snow Particles: Supporting Habit-Dependent Growth Models and Radar Applications (McRadar 1.0. 0), Geoscientific Model Development, 19, 887–910, https://doi.org/10.5194/gmd-19-887-2026, 2026.

Welss, J.-N., Siewert, C., and Seifert, A.: Explicit habit-prediction in the Lagrangian super-particle ice microphysics model McSnow, https://doi.org/10.22541/essoar.168614461.18006193/v1, 2023.

Zawadzki, I.: Observations of snow growth by a vertically pointing radar, in: 36th Conf. on Radar Meteorology, 2013.

Zawadzki, I., Fabry, F., and Szyrmer, W.: Observations of supercooled water and secondary ice generation by a vertically pointing X-band Doppler radar, Atmospheric Research, 59-60, 343–359, https://doi.org/10.1016/S0169-8095(01)00124-7, 2001.